SAND2000-0804J

THREE-PHASE MATERIAL DISTRIBUTION MEASUREMENTS IN A VERTICAL FLOW USING GAMMA-DENSITOMETRY TOMOGRAPHY AND ELECTRICAL-IMPEDANCE TOMOGRAPHY

D. L. George, K. A. Shollenberger, J. R. Torczynski, and T. J. O'Hern

Engineering Sciences Center

Sandia National Laboratories

Albuquerque, New Mexico 87185-0834 USA

S. L. Ceccio

Department of Mechanical Engineering and Applied Mechanics

University of Michigan

Ann Arbor, Michigan 48109-2121 USA

Submitted to the *International Journal of Multiphase Flow*

Abstract --- Experiments are presented in which electrical-impedance tomography (EIT) and gamma-densitometry tomography (GDT) measurements were combined to simultaneously measure the solid, liquid, and gas radial distributions in a vertical three-phase flow. The experimental testbed was a 19.05-cm diameter bubble column in which gas is injected at the bottom and exits out the top while the liquid and solid phases recirculate. The gas phase was air and the liquid phase was deionized water with added electrolytes. Four different particle classes were investigated for the solid phase: 40-100 μm and 120-200 μm glass beads (2.41 g/cm^3), and 170-260 μm and 200-700 μm polystyrene beads (1.04 g/cm^3). Superficial gas velocities of 3 to 30 cm/s and solid volume fractions up to 0.30 were examined. For all experimental conditions investigated, the gas distribution showed only a weak dependence on both particle size and density. Average gas volume fraction as a function of superficial gas velocity can be described to within ±0.04 by a curve passing through the center of the data. For most cases the solid particles appeared to be radially uniformly dispersed in the liquid.

Key Words: gamma-densitometry tomography, electrical-impedance tomography, bubble column, gas volume fraction, multiphase flow

DISCLAIMER

DISCLAIMER

Portions of this document may be illegible in electronic image products. Images are produced from the best available original document.

1. INTRODUCTION

The spatial distribution of materials in multiphase flows is important to many chemical and industrial processes. For example, a bubble column reactor is used in indirect coal liquefaction in which a reactive gas is bubbled through a catalyst-laden slurry; a spatially nonuniform gas distribution within the reactor can reduce process efficiency by inducing large-scale, buoyancy-driven recirculating flows (Jackson *et al.,* 1996). Techniques that measure the distribution of each phase in multiphase flows have the potential to improve the control of such processes. They also can be useful for validating computational models of multiphase flows (Plaskowski *et al.,* 1995; Torczynski *et al.,* 1997). Many ideal techniques for measuring phase distributions are based on tomographic methods that obtain data via reconstruction algorithms and probes or instruments that are placed outside the flow domain so as not to disturb the flow. Examples of these methods include gamma-densitometry tomography (GDT), electrical-impedance tomography (EIT), magnetic resonance imaging (MRI), acoustic tomography, and positron emission tomography (PET) (George *et al.*, 1998a).

GDT and other radiation-based tomographic methods are relatively mature and can accurately measure two-phase spatial distributions (Hewitt, 1978; Kumar *et al.*, 1995, Shollenberger *et al.*, 1997a). Recently, an EIT system developed at Sandia National Laboratories and the University of Michigan was validated for accurate measurements of two-phase spatial distributions (O'Hern *et al.*, 1995; Torczynski *et al.*, 1996a; George *et al.*, 2000). EIT can acquire information much more quickly than GDT and may, therefore, be useful for measuring multiphase transients. This paper documents a series of experiments in which GDT and EIT were applied simultaneously for the first time to measure time-averaged solid,

liquid, and gas radial distributions in vertical three-phase flows. Combination of these two techniques is ideal because it is relatively easy to select materials such that each technique is most sensitive to only one of the phases. For example, GDT will be most sensitive to the quantity of gas present because the radiation attenuation through each material scales with density, and EIT will be most sensitive to the quantity of conductive liquid present if both the gas and solid phases are electrically nonconducting.

The objective of this experimental study is to determine the effects that the presence of a solid phase has on three-phase distributions in bubble-column flows. The parameters for this study include gas velocity, solids volume fraction, particle size, and particle density. This paper begins with a brief introduction to the design and theory of both the GDT and EIT systems used in this study. The remaining sections of this paper describe the experimental setup, results, and conclusions.

2. EXPERIMENTAL TECHNIQUES

2.1 *Gamma-Densitometry Tomography (GDT)*

Phase distribution measurements were made with a gamma-densitometry tomography (GDT) system developed at Sandia for studies of industrial-scale multiphase flows (Torczynski *et al*, 1996b; Shollenberger *et al.*, 1997a). The GDT system has a 5-curie ^{137}Cs gamma source, a sodium-iodide scintillation detector system, a computer-controlled traverse to position the source and detector, and data acquisition hardware and software. Photons emitted by the source are collimated, pass through the experimental test section, and are then collimated again prior to reaching the detector by a 3.2-mm inside diameter lead cylinder determining the spatial extent of the measurement (Figure 1).

Measurements of the number of gamma photons observed over a set period of time (intensity, I, in counts per second) are taken along parallel beam paths. In order to increase the stability and resolution of the observed intensities, a spectrum analyzer is used to measure the energy of all photons reaching the detector. The ^{137}Cs gamma source emits monoenergetic photons with an energy of 661.6 keV, and the measured intensities are found by a curve fit to the peak surrounding this energy level. This eliminates errors resulting from drift in energy levels because of electronics, scattered photons, and background radiation.

The changes in intensity measured between any two experiments can be related to the attenuation coefficients of the media by

$$I = I_0 \exp\left[-\sum_{i=1}^{n} \mu_i L_i\right], \qquad [1]$$

where I and I_0 are the intensities with and without the attenuating media, respectively, μ_i are the attenuation coefficients (which scale with material density and are constant for a monoenergetic source), and L_i are the path lengths through each material. An attenuation coefficient averaged along each straight path through the test section, as a function of lateral location with respect to the axis, $\overline{\mu}^{ray}(x)$, can be defined for multiphase experiments as

$$\overline{\mu}^{ray}(x) = \sum_{i=1}^{n} \mu_i \, \overline{\varepsilon}_i^{ray}(x), \qquad [2]$$

where there are n phases and $\bar{\varepsilon}_i^{ray}$ is the ray-averaged volume fraction for each phase. For the experiments presented here, intensities are measured at each location with the column empty, $I_1(x)$, full of water, $I_2(x)$, and while the gas is flowing, $I(x)$. Using Equations 1 and 2, $I_1(x)$, $I_2(x)$, and $I(x)$ are translated into $\bar{\mu}^{ray}(x)$, averaged along each straight path by

$$\bar{\mu}^{ray}(x) = \mu_1 \frac{\ln[I(x)/I_2(x)]}{\ln[I_1(x)/I_2(x)]} - \mu_2 \frac{\ln[I(x)/I_1(x)]}{\ln[I_1(x)/I_2(x)]}. \quad [3]$$

Finally, $\bar{\mu}^{ray}(x)$ is normalized with respect to the gas and liquid phase attenuation coefficients, μ_1 and μ_2, respectively, to obtain

$$\psi(x) = \frac{\bar{\mu}^{ray}(x) - \mu_1}{\mu_2 - \mu_1} = \frac{\ln[I(x)/I_1(x)]}{\ln[I_2(x)/I_1(x)]}. \quad [4]$$

Thus, attenuation by the testbed walls is subtracted from the raw data; then a time-averaged, normalized radial attenuation distribution,

$$f_\mu(r) = \frac{\mu(r) - \mu_1}{\mu_2 - \mu_1}, \quad [5]$$

is reconstructed from the Abel transform of $\psi(x)$ (Vest, 1985) and the assumption of an axisymmetric phase distribution. Repeated checks of the side-to-side symmetry of the measured attenuation profiles have demonstrated that the axisymmetric assumption is valid over the long acquisition time scales of

GDT, which range from 15 to 30 minutes. In Equation 5 $\mu(r)$ is related to material volume fractions in an analogous fashion to $\overline{\mu}^{ray}(x)$ as

$$\mu(r) = \sum_{i=1}^{n} \mu_i \varepsilon_i(r), \qquad [6]$$

where $\varepsilon_i(r)$ is now the actual phase volume fraction at each radial location.

The axisymmetric attenuation and phase distributions are modeled as fourth-order polynomials using only even powers of r as shown for $f_\mu(r)$:

$$1 - f_\mu(r) = a_0 + a_1\left(\frac{r}{R}\right)^2 + a_2\left(\frac{r}{R}\right)^4. \qquad [7]$$

Two special cases of interest arise when phase 1 is a gas, μ_1 is negligible, and either of the following apply: (1) there are only two phases ($n = 2$), or (2) there are three phases ($n = 3$) and the remaining two phases have the same attenuation coefficient ($\mu_2 = \mu_3$). Then the following relationships can be derived from Equations 2 through 6 between gas volume fraction, $\overline{\varepsilon}_G^{ray}(x)$ or $\varepsilon_G(r)$, the normalized-ray attenuation coefficient, $\psi(x)$, and the normalized attenuation coefficient, $f_\mu(r)$:

$$\overline{\varepsilon}_G^{ray}(x) = 1 - \psi(x) \quad \text{and} \quad \varepsilon_G(r) = 1 - f_\mu(r). \qquad [8]$$

Thus, for these two cases gas volume fraction can be measured directly with GDT. For three-phase flows if the attenuation coefficients are different for each phase, additional information is required to resolve all three-phase volume-fraction profiles.

2.2 *Electrical-Impedance Tomography (EIT)*

Additional phase distribution measurements were made with an EIT system developed collaboratively by Sandia National Laboratories (Torczynski *et al.*, 1997; George *et al.*, 1998b) and the University of Michigan that has been calibrated for two-phase measurements using the Sandia GDT system. Details of the design and implementation of this system have been described in detail by George *et al.* (2000) and will be summarized here. The EIT system consists of an electrode array; a signal generator; a voltage-controlled current source; multiplexers connecting the electrode array to the current source, ground, and measurement electronics; an instrumentation amplifier and phase-sensitive demodulators; a low-pass filter to eliminate high-frequency components from the demodulated signals; and a data acquisition card. The data acquisition card contains an analog-to-digital converter that measures the DC signal components and a digital controller that can be used to select electrodes for current injection, ground, and measurement. The card also acts as an interface to a PC that operates the entire system.

During operation the EIT system injects a controlled current through one electrode, "sinks" a second electrode to ground, and measures voltages at all electrodes relative to ground as shown schematically in Figure 2. For completeness a "projection set" consists of measurements at all N electrodes for each injection and ground combination, for a total of $N^2(N-1)/2$ voltage measurements.

Note that this is a factor of N greater than the number of independent pieces of information, $N(N-1)/2$; the extra information is used to reduce the impact of noise on the reconstructions. The domain is excited with a 50-kHz AC electric field. The resistive component of impedance dominates at this frequency for the air-water-polystyrene and air-water-glass flows considered here.

The voltage signal from each electrode passes through an amplifier to a pair of phase-sensitive demodulators that separate the measured signal into two components: one demodulator produces the component in phase with the EIT carrier signal, and the other yields the quadrature component out of phase with the carrier by 90°. Because the demodulators multiply two 50-kHz signals together (the measured voltage and the carrier or quadrature reference signal), their outputs consist of a 100-kHz sine wave superimposed on a DC component. The sine wave is removed by the low-pass filter, yielding the DC component proportional to the carrier or quadrature component of the measured voltage.

The electrode array discussed in this paper and shown in Figure 3 was fabricated for use both in validation tests and in experiments conducted in the transparent bubble column (Section 3.1). The 16 electrodes were made from stainless steel strips 0.64 cm wide, 7.62 cm high, and 76 μm thick. These were mounted at equal azimuthal intervals in a Lucite cylinder with an inner diameter of 19.05 cm, a wall thickness of 0.64 cm, and a height of 12.7 cm. For 16 electrodes the acquisition time for each voltage projection set is either 0.5 seconds using integrated circuit counters or 1.5 seconds using a software-controlled command option. Validation tests presented in George *et al.* (2000) demonstrated that the choice of mode has little impact on reconstruction accuracy.

In electrical-impedance tomography the measurements at the domain boundary are used to reconstruct the impedance distribution within the domain and to infer the phase distribution. For AC

electrical conduction with field frequencies on the order of tens of megahertz or lower, the electric potential, V, within the domain, **D**, is related to the complex electrical conductivity, $\gamma = \sigma + i\omega$, of the domain by

$$\nabla \cdot \gamma \nabla V = 0. \qquad [9]$$

Equation 9 assumes that no charge sources or sinks are present in **D**. The boundary conditions on **D** are given by

$$\mathbf{n} \cdot \gamma \nabla V + j = 0, \qquad [10]$$

where **n** is the unit normal vector outward from the domain boundary, and j is the charge flux on the boundary. Multiple measurements of j and V at the boundary are used to iteratively reconstruct the conductivity distribution within **D** that yields the measured boundary conditions. More information on EIT theory and the development of EIT systems for the study of multiphase flows may be found in Dickin *et al.* (1993); Jones *et al.* (1992, 1993, 1994); and Ceccio and George (1996).

The reconstruction algorithm used with the Sandia EIT system has been described in detail by Torczynski *et al.* (1996a, 1997) and is based on the YWT method described by Yorkey *et al* (1987). The algorithm is summarized here. In the algorithm the medium is treated as purely resistive, with no capacitive contribution. Thus, the complex electrical conductivity is replaced by the conductivity in Equations 9 and 10 ($\gamma \rightarrow \sigma$). The medium is surrounded by an insulating boundary through which

current is injected or withdrawn at discrete electrodes. A finite-element method (FEM) representation is generated for the voltage equation, identical in form to the steady-state heat-conduction equation. Unlike most finite-element methods, the conductivity is not represented by a piecewise-constant function that is discontinuous at element boundaries. Instead, the electrical conductivity is represented as a global function of position and of one or more conductivity parameters. Current flow is specified at the electrodes for the boundary conditions such that the net current into and out of the domain is zero.

The finite-element equations generated from Equations 9 and 10 are solved to find both the predicted voltages at the electrodes and the derivatives of the electrode voltages with respect to the conductivity parameters. Subsequently, the conductivity parameters are adjusted by a Newton-Raphson algorithm to minimize the least-squares difference between the computed and experimental electrode voltages at the noncurrent-bearing electrodes. Since no voltages are prescribed in the computational boundary conditions, the computed voltage solution of Equation 9 is unique only to within an arbitrary additive constant. The value of the additive constant is determined during the least-squares minimization process (see George *et al.*, 2000). The code written to implement this approach models cylindrical domains within which the conductivity varies only radially, but the voltage fields vary three-dimensionally to reflect the finite axial extent of the electrodes. The calculated conductivity field is represented as a global function of radial position and of conductivity parameters. The following representation of a quartic radial conductivity profile was chosen:

$$\frac{\sigma(r)}{\sigma_L} = \frac{1 + C_1\left(2\tilde{r}^2 - 1\right) + C_2\left(1 - 6\tilde{r}^2 + 6\tilde{r}^4\right)}{C_0}, \qquad [11]$$

where σ_L is the liquid phase conductivity, C_1 and C_2 are the conductivity shape parameters, C_0 is a scale parameter, $\tilde{r} = r/R$, r is the radial coordinate, and R is the radius of the circular domain.

A constitutive model is required to relate the electrical conductivity to the conducting and insulating phase volume fractions. When the continuous liquid phase is the only conducting phase, the Maxwell-Hewitt relation (Maxwell, 1881; Hewitt, 1978) can be used to relate the mixture conductivity, σ, and the liquid conductivity, σ_L, to the insulating phase volume fraction, ε_I:

$$\frac{\sigma}{\sigma_L} = E(\varepsilon_I, \alpha), \quad E(\xi, \eta) = \frac{1-\xi}{1+\eta\,\xi}. \qquad [12]$$

In Equation 12 the parameter $\alpha = 1/2$ for three-dimensional inclusions of an insulating phase dispersed in a conducting phase (*e.g.*, bubbles or insulating solid particles in salt water). An analogous relation can be derived for the somewhat artificial case of two-dimensional insulating inclusions dispersed in a conducting phase (*e.g.*, parallel insulating posts in salt water) by using $\alpha = 1$ in Equation 12. Validation experiments in two-phase churn-turbulent bubble-column flows by George *et al.* (2000) showed that $\alpha = 3/5$ provided the best agreement between the EIT and GDT profile data. The parameter, α, may lie between the two extreme cases because of the vertical motion or axial elongation of the bubbles during each measurement period. Thus, $\alpha = 3/5$ was used to approximately account for the axial motion of the insulating phases in Equation 12 for all of the results presented here. An additional modification to Equation 12 can be made to account for a bimodal particle size distribution (i.e. two insulating phases of different sizes). The details of this modification will be presented in Section 4.1, where the method for combining the GDT and EIT reconstructions is presented for these experiments.

3. EXPERIMENTAL SETUP

3.1 *Testbed setup*

The three-phase experiments were conducted in a vertical bubble column, shown schematically in Figure 4. The column is constructed of transparent Lexan with an inside diameter, D, of 19.05 cm and a wall thickness of 0.64 cm. It is built from interchangeable sections so that different diagnostics can be placed in the column. In each three-phase experiment the column was initially filled with water and solids to a depth, H, of 144.8 cm, for a height-to-diameter ratio of $H/D = 7.6$. The 16 strip electrodes were centered on a plane $L = 82.0$ cm above the base ($L/D = 4.3$), placing the region of EIT sensitivity completely under water. GDT scans were taken on two source-detector planes located at $L = 70.6$ and 93.4 cm above the column base ($L/D = 3.7$ and 4.9). These positions above and below the midplane of the EIT electrode ring were chosen to prevent obstruction by the electrodes, the cables exterior to the electrode ring, and the O-ring collars that joined the electrode ring to the remainder of the column. These locations also allowed verification that fully developed flow had been achieved at the measurement region.

A ring sparger was used to introduce dry air into the flow near the bottom of the column. The sparger is a hollow stainless steel toroid with a 10.16-cm centerline diameter, a tube-inner diameter of 0.95 cm, and 10 evenly spaced holes of 0.16 cm diameter. The sparger holes were pointed towards the bottom of the column to loft the solids from the column floor. For the initial experiments with the 200-700 μm polystyrene particles, the sparger was located approximately 13 cm above the base of the

column. To improve the lofting efficiency of the sparger for the denser glass spheres, the sparger was lowered to a position 6 cm above the base of the column. All tests were conducted at ambient pressure. Three cartridge heaters along the height of the column were used to counteract evaporative cooling and maintain a constant temperature. The liquid temperature was held constant to within ±0.4 °C during experiments, which limited conductivity variations induced by temperature to ±0.6%.

3.2 *Material Properties*

The material properties of the phases used in these experiments are presented in Table 1. Deionized water was used as the liquid phase, with controlled amounts of sodium nitrate added to increase conductivity well above the lower limit for the EIT system of 200 μS/cm and to provide a useful dynamic range of measured voltages. The initial DC conductivity of the aqueous sodium nitrate solution, measured before the first test at each solid loading, was $\sigma_L = 261 \pm 19$ μS/cm. As will be discussed in the following section, the conductivity consistently increased over the course of experiments as gas-liquid circulation removed more coating material from the solids. The attenuation coefficient of glass in Table 1 was measured with the GDT system itself to account for unknown quantities of impurities (Shollenberger *et al.*, 1997b), whereas the attenuation coefficients of polystyrene, air, and water were obtained from the literature (Lamarsh, 1983; Thoraeus, 1965). The density of air was calculated assuming it is an ideal gas at a pressure determined by the depth of the EIT measurement plane and at the controlled temperature. The value of the gas density varied by less than 2.5% over the extent of the GDT and EIT measurement planes ($L/D = 1.2$) which corresponds to similar changes in the attenuation

coefficient. These changes were assumed negligible for the phase volume fraction calculations because the gas attenuation coefficient is much less than that of the liquid and solid phases.

To determine whether density and size distribution of the solid particles can affect the behavior of the other phases, experiments were performed with a total of four different types of particles. The particles were chosen so that the effects of size and density could be observed separately. Polystyrene beads, with a density a 1.04 g/cm^3, were chosen with nominal diameters of 200 and 400 μm. Glass beads, with a density of 2.41 g/cm^3, were chosen with nominal diameters of 80 and 200 μm. The solid densities were measured by a volumetric method.

Plots of the size distribution for each type of particle are shown in Figures 5 through 8. From pictures of the particles, it is apparent that some of the "small" glass particles are decidedly aspherical; most are globular, but some elongated particles and shards are present. By comparison, the other particles are almost uniformly spherical. The graphs in each figure show the size distribution of each particle type, both in terms of number percentage and volume percentage, as determined by using a Mie-scattering technique. The size distribution of the "large" polystyrene particles is seen to be broadest by far, with 98% of the volume of solids consisting of particles with diameters in the range of 200-700 μm. The "small" glass beads, the second type of particles to be investigated, are seen to have diameters generally in the range of 40-100 μm. The "medium" glass and polystyrene particles were identified by their respective manufacturers as nominally 200 μm in diameter but had notably different distributions: 120-200 μm for the glass spheres, 170-260 μm for the polystyrene.

3.3 *Experimental Procedure*

The polystyrene particles were washed and rinsed repeatedly to minimize the amount of soluble contamination carried by the solids into the liquid before the first set of three-phase experiments were conducted. Despite these efforts, noticeable amounts of opaque coating material were transferred from the polystyrene particles into the liquid by the turbulent flow. The opaque coating acted as a surfactant, as evidenced by foam at the top of the liquid column during gas flow. Electrolytes present in the coating material also altered the liquid conductivity over the course of experiments. To compensate for the effect of the contaminants, a standard procedure of using the EIT system itself to measure the baseline liquid conductivity between tests was followed. The glass spheres also shed opaque material into the liquid during experiments. Although the glass particles were not washed before tests, the conductive effects of their contaminant were much less than that of the polystyrene, suggesting that a different coating was involved or perhaps that the "contaminant" was very small shards of broken particles. Again, baseline EIT conductivity measurements taken between flow conditions were used to compensate.

Table 2 lists the combinations of solid materials, solids loading, and superficial gas velocities at which measurements of phase distributions were made. The superficial gas velocity, U_G, is defined as the velocity the gas would have if it moved through the column alone ($U_G = \dot{m}_G / (\rho_G A)$, where $\dot{m}_G$ is the gas mass flow rate, ρ_G is the gas density, and A is the column area). Experiments were broken into subsets, each involving one nominal slurry concentration, $\bar{\varepsilon}_S^{nom}$, defined as the ratio of the total volume of solid particles to the combined reference volume of the liquid and solid particles. Slurry concentrations up to $\bar{\varepsilon}_S^{nom} = 0.30$ were included in the tests with large polystyrene particles; concentrations for the other solids were limited to $\bar{\varepsilon}_S^{nom} = 0.15$, the highest loading of glass particles that

could be completely lofted for these gas velocities. To obtain the desired slurry concentrations for each subset, the total mass of required particles was computed from the reference volume (41.26 L, based upon a depth of $H = 144.8$ cm) and the known density of the solid material. Any amount of solids already present in the column from previous experiments was subtracted from this total to find the mass to be added. This mass was weighed out, introduced into the column, and allowed to settle to the bottom. After settling of the solids, liquid was drained from the column to return the total solid-liquid volume to the reference value, and an EIT scan was performed to measure the baseline liquid conductivity.

The downward flow of air from the sparger was sufficient to loft all of the solids from the bottom and produce a three-phase flow throughout the column in each successful test. No measurements were made for certain combinations of gas flow rate and solid volume fraction, marked "a" in Table 2, because an appreciable amount of solid particles remained at the bottom of the column under these conditions. Although these particles could be lofted temporarily by increasing the gas velocity, they settled to the bottom of the column when the gas velocity was returned to the prescribed value. Lofting efficiency was influenced both by particle density and to some extent by particle diameter. It should be noted that cases of "0%" nominal slurry concentration employ water in which solids previously added were removed for the test, leaving coating material in the water. This was necessary to ensure that the surface tension was the same for all experiments, both with and without solids present. Table 2 also notes flow conditions that were attempted but not completed because the surfactant foam above the solid-liquid slurry expanded and threatened to overflow the top of the column.

Profile measurements at each flow condition consisted of a GDT scan at the lower scan plane, followed by an EIT scan, followed by a second GDT scan at the upper plane. After the profile

measurements were completed at each condition, gas flow was terminated, and the solids were allowed to settle well beyond the EIT measurement region to the bottom of the column. This settling process required 15 to 60 minutes, depending upon the amount and type of solids present. Following the settling period EIT was applied again to measure changes in the baseline conductivity of the liquid. The values of liquid conductivity measured before and after each set of flow conditions were averaged and used to compute volume fraction profiles under those conditions. In the polystyrene experiments a fraction of the particles floated to the free surface of the liquid during the settling period. This layer of solids was not disturbed during the settling period or the EIT baseline measurements but was forced back into the liquid before the next test.

The information from the pair of GDT scans was averaged and combined with the EIT data to determine the radial volume fraction profiles at the EIT electrode plane for each flow condition. Each GDT scan included data acquisitions for 60-second periods along 19 parallel beam paths that spanned from one side of the column to the other. Thus, GDT reconstructions were averages over a period of 23 minutes. Based on an analysis of the GDT technique from Shollenberger *et al.* (1997a), the uncertainty for each gas volume fraction data point for these experiments is estimated to be ±0.01. The two GDT scans above and below the EIT ring did not differ from each other by more than 0.01 in gas volume fraction at each radial location, supporting the assumption of a fully developed flow at the measurement plane.

For the first experiments with the 200-700 μm polystyrene particles, 25 EIT projection sets were acquired in the fast mode (integrated circuit counters, 0.5 seconds per EIT projection) during each flow condition over a period of about 20 seconds and averaged to yield voltage data for reconstructions. After

the first polystyrene experiments, uncertainty analyses of the quartic EIT reconstruction algorithm showed that a total of 100 projection sets should be collected and averaged for the remaining tests. A second change was that the data acquisition was now performed in the slow mode (software controlled, 1.5 s per EIT projection). As a result, EIT reconstructions for the remaining tests represented averages over a period of 2.5 minutes. George *et al.* (2000) demonstrated that the differences in temporal averaging by GDT and EIT did not significantly affect the results for two-phase bubble column flows for superficial gas velocities up to 8.8 cm/s. They also showed that measurements of gas volume fraction using EIT did not differ from the GDT results by more than 0.01 at any radial location. Based on the accuracy of each of the EIT and GDT systems, it is expected that the accuracy of the combined techniques for estimating all three-phase volume fractions should be approximately ±0.02.

4. RESULTS AND DISCUSSION

4.1 *Calculation of phase volume fraction profiles*

This section presents the relations used in this study to determine the radial variations of the gas, liquid, and solid volume fractions ($\varepsilon_G(r)$, $\varepsilon_L(r)$, and $\varepsilon_S(r)$, respectively) from the radial variations of the normalized gamma attenuation, f_μ, the normalized electrical conductivity, $\sigma(r)/\sigma_L$, and the total volume relationship:

$$\sum_{i=1}^{n} \varepsilon_i(r) = 1. \qquad [13]$$

The only additional information needed to calculate $\varepsilon_G(r)$, $\varepsilon_L(r)$, and $\varepsilon_S(r)$ are four physical properties known *a priori*: the phase attenuation coefficients, μ_S, μ_L, and μ_G, listed in Table 1 and the liquid conductivity, σ_L, measured with the EIT system. For the churn-turbulent bubble column flow investigated in this paper, two different ways of applying the Maxwell-Hewitt relation (Equation 12) have been considered.

For the simple case where the quantity $\varepsilon_I(r)$ in Equation 12 is set equivalent to the total insulating phase fractions, $\varepsilon_I(r) = \varepsilon_G(r) + \varepsilon_S(r) \doteq 1 - \varepsilon_L(r)$, $\varepsilon_L(r)$ can be solved for directly from Equation 12 as

$$\varepsilon_L(r) = \frac{(1+\alpha)\sigma(r)/\sigma_L}{1+\alpha\,\sigma(r)/\sigma_L}. \qquad [14]$$

Calculation of the gas volume fraction from $\varepsilon_L(r)$ and GDT data is derived from Equations 5 and 6 as

$$\varepsilon_G(r) = 1 - \left(\frac{\mu_L - \mu_G}{\mu_S - \mu_G}\right) f_\mu(r) - \left(\frac{\mu_S - \mu_L}{\mu_S - \mu_G}\right) \varepsilon_L(r). \qquad [15]$$

Finally, $\varepsilon_S(r)$ is calculated using Equation 13.

The second implementation of the Maxwell-Hewitt relation is a little more complicated. As discussed in George *et al.* (2000), the Maxwell-Hewitt relation can be modified to represent a bimodal distribution of "particle" sizes (*i.e.*, large bubbles and small solid particles) by treating the three-phase flow as gas bubbles within a liquid-solid mixture. In this case the modified Maxwell-Hewitt relation is

applied recursively, first to the solid particles in the liquid phase, then to the gas in the liquid-solid mixture. The following relation replaces Equation 14:

$$\frac{\sigma(r)}{\sigma_L} = E\left[\varepsilon_G(r), \alpha\right] E\left[\frac{\varepsilon_S(r)}{\varepsilon_S(r)+\varepsilon_L(r)}, \alpha\right]. \qquad [16]$$

Obviously, Equation 16 can no longer be solved directly for $\varepsilon_L(r)$, so Equations 13, 15, and 16 must now be solved simultaneously to calculate each volume fraction profile. A closed-formed solution is still found as follows:

$$\varepsilon_G(r) = \frac{-b(r) + \sqrt{b(r)^2 - 4a(r)\,c(r)}}{2a(r)} \qquad [17]$$

$$a(r) = 1 + \left[\left(\frac{\mu_S - \mu_L}{\mu_S - \mu_G}\right)\alpha - \left(\frac{\mu_L - \mu_G}{\mu_S - \mu_G}\right)\alpha^2\right]\frac{\sigma(r)}{\sigma_L}$$

$$b(r) = -2 + \left(\frac{\mu_L - \mu_G}{\mu_S - \mu_G}\right) f_\mu(r) + \left\{\left(\frac{\mu_S - \mu_L}{\mu_S - \mu_G}\right) - \alpha + \left(\frac{\mu_L - \mu_G}{\mu_S - \mu_G}\right)\left[1 - f_\mu(r)\right]\alpha^2\right\}\frac{\sigma(r)}{\sigma_L}$$

$$c(r) = 1 - \left(\frac{\mu_L - \mu_G}{\mu_S - \mu_G}\right) f_\mu(r) + \left\{-\left(\frac{\mu_S - \mu_L}{\mu_S - \mu_G}\right) + \left(\frac{\mu_L - \mu_G}{\mu_S - \mu_G}\right)\left[1 - f_\mu(r)\right]\alpha\right\}\frac{\sigma(r)}{\sigma_L}$$

$$\varepsilon_L(r) = \left(\frac{\mu_S - \mu_G}{\mu_S - \mu_L}\right) - \left(\frac{\mu_L - \mu_G}{\mu_S - \mu_L}\right) f_\mu(r) - \left(\frac{\mu_S - \mu_G}{\mu_S - \mu_L}\right)\varepsilon_G(r). \qquad [18]$$

Once again $\varepsilon_S(r)$ is calculated using Equation 13. Because this modified Maxwell-Hewitt relation is more appropriate for the "bimodal" mixture (small particles and large bubbles) found in these experiments, it was used to calculate all the profiles in this paper.

The independent measurement of slurry concentration, $\bar{\varepsilon}_S^{nom} = V_S/(V_S + V_L)$, can be used to check the modified Maxwell-Hewitt relation by comparing it to the slurry concentration at the measurement plane calculated by integrating the profiles using Simpson's Rule, as shown in Figure 9. First, a baseline case for each particle type and gas flowrate was acquired where $\bar{\varepsilon}_S^{nom} = 0$. Although the calculations did not force the measured slurry concentration to be zero for these cases, the slurry concentration was calculated to be less than 0.01 for superficial gas velocities less than about 10 cm/s and less than 0.03 for higher velocities. Thus, there is a slight bias in the slurry concentration possibly owing to temporal-averaging errors at higher gas velocities. Recall from Equation 8, however, that this bias has almost no effect on the measured gas volume fraction for the polystyrene particle cases because the attenuation coefficients for the solid and the liquid phases are almost the same. The effect of this bias on the gas volume fractions for the glass particle cases is uncertain.

Figure 9 shows that for the polystyrene particle cases, with nominal slurry concentrations from 0.05 to 0.30, the measured slurry concentrations increase slightly towards $\bar{\varepsilon}_S^{nom}$ and then above it as the superficial gas velocity increases. It is likely that the overprediction is owing to the bias mentioned above. For the cases where the denser glass particles are used, the measured slurry concentrations are generally lower than those for the polystyrene particles, particularly at the higher nominal slurry concentrations. Also, as the glass particle size increases, the measured slurry concentration decreases. The lowered slurry concentrations are most likely owing to partial lofting of the higher density particles

which increases with particle size. Based on these results it is concluded that the modified Maxwell-Hewitt relation reasonably predicts the slurry concentrations for these experiments to within an accuracy of approximately ±0.03.

4.2 *Three-phase results*

The first parameter investigated is superficial gas velocity. Figures 10 (a) through (d) show phase volume fraction profiles for four superficial gas velocities for the 170-260 μm polystyrene particles at a nominal slurry concentration, $\bar{\varepsilon}_S^{nom}$, of 0.10. Several general observations can be made about the results. First, as expected, the gas volume fraction increases as the superficial gas velocity is increased. The gas volume fraction profiles behave like those found in churn-turbulent gas-liquid flows, increasing with U_G preferentially on the column axis (Joshi *et al.*, 1998). Based on visual observations, the flows were all in the churn-turbulent regime for the range of gas velocities studied. At higher gas flow rates, large non-spherical bubbles were occasionally visible at the column walls. As expected, the profiles of $\varepsilon_L(r)$ are shown to decrease with increasing U_G as the liquid phase is displaced by the gas phase. The profiles of $\varepsilon_s(r)$ remain approximately constant in magnitude and are mostly flat with a slight increase at the walls. However, examining solids profiles for all of the cases studied reveals profile shapes that include concave upward, concave downward, and a maximum at a radial location between the axis and the wall. In most cases these variations lie within or close to the indicated uncertainty and should not be considered significant.

The second parameter of interest is nominal slurry concentration, $\bar{\varepsilon}_S^{nom} = V_S/(V_S + V_L)$. Figures 11 (a) through (d) show phase volume fraction profiles at four different values of $\bar{\varepsilon}_S^{nom}$ for the 120-200 μm glass particles at 17.5 cm/s superficial gas velocity. As expected, the magnitude of the profiles of $\varepsilon_S(r)$ is seen to increase with nominal slurry concentration. The shape of the profiles of $\varepsilon_S(r)$ evolves from a maximum at a radial location between the axis and the wall to concave upward, but as noted above, these changes are within the indicated uncertainty and may not be significant. The shape and magnitude of the profiles of $\varepsilon_G(r)$ are almost identical in all four plots to within ±0.03. Indeed, for the polystyrene particles at each gas flow rate examined, the shape of the gas volume fraction radial profile was also unaffected by the addition of solids to within ±0.03 in volume fraction. Finally, because $\varepsilon_S(r)$ is increasing while $\varepsilon_G(r)$ remains relatively constant, $\varepsilon_L(r)$ is found to decrease accordingly as the solid displaces the liquid.

The effect of particle density on the phase volume fraction profiles can be considered by comparing results from studies with the 170-260 μm polystyrene particles and the denser 120-200 μm glass particles. In general, Figures 10 (a) through (d) for the polystyrene particles show that the profiles of $\varepsilon_G(r)$ are rounded or parabolic in shape. Figures 11 (a) through (d) for the glass particles show that the profiles of $\varepsilon_G(r)$ are noticeably flatter at the center of the column or quartic in shape. The blunter profile for the glass particles may be caused by the increased inertia of the slurry which enhances bubble breakup and produces a more homogeneous, plug-like flow. However, the changes in profile shape may again be within the experimental uncertainty for these experiments. In addition, recall that the gas volume fraction profiles for the polystyrene particles are calculated mainly from GDT alone (Equation

8) and for the glass particles are calculated from the combined EIT and GDT equations. In contrast to the above results, the profile shapes of the GDT function, $f_\mu(r)$, between the two particle types do not change noticeably. Thus, the changes in the profiles observed here between the glass and polystyrene particles must be caused by the fourth-order term in the EIT reconstruction which has the highest degree of uncertainty for these measurements.

The effect of particle size on phase volume fraction profiles can be examined for both particle types. Figure 12 shows phase volume fraction profiles where the solid phase is 40-100 μm glass beads for a superficial gas velocity of 17.5 cm/s and a nominal slurry concentration of 0.10. This can be compared to Figure 11 (c) for the 120-200 μm glass particles at the same flow conditions. All three of the profiles in these figures are very similar in shape. Figure 13 shows phase volume fraction profiles for which the solid phase is 200-700 μm polystyrene beads, with a superficial gas velocity of 11.7 cm/s and a nominal slurry concentration of 0.10. This can be compared to Figure 10 (b) for the 170-260 μm polystyrene particles at the same flow conditions. Again, all of the profiles in these figures are very similar. Changes in the magnitudes between these plots are hard to discern; to consider these small changes, radially averaged data were computed from the reconstructions using Simpson's Rule to integrate the profiles. One benefit of looking at the radially averaged data is that more accurate results can be obtained for the averages than for the individually reconstructed data points (Mwambela *et al.*, 1997).

The effect of the presence of solids on average gas volume fraction, $\bar{\varepsilon}_G$, is quantified in Table 2 and in Figure 14, which show $\bar{\varepsilon}_G$ as a function of superficial gas velocity, U_G, for all four particle types. For comparison Figure 14 also shows average gas volume fractions obtained using clean, deionized water and no solids. In all cases $\bar{\varepsilon}_G$ is seen to increase monotonically with U_G, as expected. A nominal solid

volume fraction of 0% in these graphs indicates cases in which particles loaded for previous experiments have been removed from the water, leaving particle surface coating material behind. These volume fractions are considerably lower than for the cases in which particles are employed, but all results can be described to within ±0.04 by a curve passing through the middle of the data. As noted earlier, the addition of particles also unavoidably adds surfactants that reduce surface tension and change the gas volume fraction, $\bar{\varepsilon}_G$, by +0.02 to +0.06, substantially more than the change produced by the particles themselves.

In order to see the effects of particle diameter and density more clearly, the data in Figure 14 are plotted separately in Figures 15 and 16 for each particle type as a function of nominal slurry concentration. The average gas volume fractions in these experiments are roughly independent of particle diameter for the glass particles (Figure 15). However, for the 170-260 μm polystyrene particles, increases in $\bar{\varepsilon}_G$ of up to 0.04 are observed for nominal slurry concentrations greater than 0.05 (see Figure 16). Decreases in $\bar{\varepsilon}_G$ with increasing solids density are also evident from these experiments. The plot for glass particles (Figure 15) shows a clear decrease in gas volume fraction (by as much as 0.04 in $\bar{\varepsilon}_G$) with increasing solid volume fraction, but no such trend is observed for the polystyrene particles (Figure 16).

4.3 *Average Gas Volume Fraction Correlation*

Typically, average gas volume fraction measurements in bubble-column flows are correlated using three liquid properties: density, viscosity, and surface tension. Greater liquid density increases the buoyant force on a bubble, which increases its velocity relative to the liquid and thereby tends to

decrease the gas volume fraction. However, greater liquid density also increases its inertia which enhances bubble breakup, reduces bubble size and velocity relative to the liquid, and thereby tends to increase the gas volume fraction. A majority of the empirical gas-liquid correlations in the exhaustive review by Joshi *et al.* (1998) indicate that increasing liquid density generally increases gas volume fraction. This suggests that the bubble breakup effect of the liquid density tends to dominate in bubble column reactors. Similarly greater liquid viscosity decreases bubble velocity but increases bubble size; in this case the latter effect dominates, and the net result is generally a reduction in gas volume fraction. Finally, greater surface tension generally increases bubble size and thereby reduces gas volume fraction. These opposing trends with liquid properties are supported by the common dependence in empirical correlations of gas volume fraction on the Morton, Weber, and Reynolds numbers, which can be defined respectively as follows:

$$\mathrm{Mo} = \frac{g\,\eta_L^4\,(\rho_L - \rho_G)}{\rho_L^2\,\sigma^3}, \qquad [19]$$

$$\mathrm{We} = \frac{U_G^2\,D\,\rho_L}{\sigma}, \qquad [20]$$

$$\mathrm{Re} = \frac{U_G\,D\,\rho_L}{\eta_L}. \qquad [21]$$

where ρ_L is liquid density, ρ_G is gas density, η_L is liquid dynamic viscosity, σ is surface tension (not to be confused with the electrical conductivity), D is column diameter, and g is the acceleration owing to gravity.

One simple way to correlate the three-phase data presented in this paper is to assume that the solid is uniformly dispersed in the liquid and that the slurry behaves as a single phase with the properties of the suspension. The effective density and viscosity can be easily adjusted to account for the presence of the solid phase. The effective density can be calculated as

$$\rho = \bar{\varepsilon}_S^{nom} \rho_S + \left(1 - \bar{\varepsilon}_S^{nom}\right) \rho_L, \qquad [22]$$

where ρ_S is solid density, and the effective viscosity can be calculated using a correlation for a suspension from Thomas, (1965) as

$$\frac{\eta}{\eta_L} = 1 + 2.5\,\bar{\varepsilon}_S^{nom} + 10.05\,\bar{\varepsilon}_S^{nom^2} + 0.00273\exp\left(16.6\,\bar{\varepsilon}_S^{nom}\right). \qquad [23]$$

Note that this correlation does not account for particle size, assumes a uniform size distribution of particles, and is valid for particle volume fractions up to 0.25. The changes in surface tension are much harder to account for, so the surface tension of the electrolyte solution was measured for each experiment and found to decreased by 2 to 20 dynes/cm. A strictly empirical correlation based on a non-dimensional analysis was used to fit the experimental data in Figures 15 and 16,

$$\bar{\varepsilon}_G = C\mathrm{Mo}^{m_1}\left(\frac{\rho_G}{\rho}\right)^{m_2}\left(\frac{\mathrm{We}}{\mathrm{Re}}\right)^{m_3}, \qquad [24]$$

where $C = 2.1069$, $m_1 = -0.1193, m_2 = 0.3507$, and $m_3 = 0.4757$. The calculated curves are also shown in Figures 15 and 16. For the glass beads (Figure 15), the correlation generally reproduces the data except at the lowest superficial gas velocity. Also, the data from the 200-700 μm polystyrene particles (Figure 16) show excellent agreement with the correlation. However, the data from the experiments with 170-260 μm polystyrene particles are not fit well by the correlation.

5. CONCLUSIONS

The application of tomographic techniques to multiphase flows continues to be a significant research topic for which goals include improvements in temporal and spatial resolution, quantitative accuracy, and use in a broader class of multiphase flows. In a contribution to this field, a gamma-densitometry tomography (GDT) system and an electrical-impedance tomography (EIT) system, developed collaboratively by Sandia National Laboratories and the University of Michigan, have been combined to measure three-phase volume fractions in vertical flows. The goal of these experiments was to examine the effect of the solid phase on the three-phase distributions in bubble-column flows. The study employed solid phases with conductive properties similar to air but densities on the same order of magnitude as water, so that each of the three phases involved a unique combination of attenuating and conductive properties. This also required that the constitutive equations for both measurement methods be solved simultaneously to determine the distributions of all three phases. Four particle types were examined: 40-100 μm and 120-200 μm glass beads (2.4 g/cm^3), and 170-260 μm and 200-700 μm polystyrene beads (1.04 g/cm^3). Nominal slurry concentrations, $\bar{\varepsilon}_S^{nom} = V_S/(V_S + V_L)$, of up to 0.30 were

examined over superficial gas velocities in the 2-30 cm/s range. Experiments with solid particles of different sizes and densities were performed to determine the influences of these quantities on phase volume fraction profiles.

Over the range of nominal slurry concentrations from 0 to 0.30, the gas distribution for each gas flow rate was relatively insensitive to the amount of solids present in the mixture. For all of the particle types that were examined, a maximum variation in gas volume fraction of ±0.04 was observed for a given superficial gas velocity. The neutrally buoyant 200-700 μm polystyrene particles were found to have almost no effect on the gas distribution. A slight increase in gas volume fraction with nominal slurry concentration was measured for the 170-260 μm polystyrene particles. No particle size effect was measured for the glass particles. A slight decrease in gas volume fraction with nominal slurry concentration was observed with the glass particles, which were substantially denser than the liquid. The physical mechanism responsible for this effect is not yet clear. By comparison, surface-tension changes from contaminants added with the particles were more important than changes from the presence of the particles themselves. Finally, the particles appear to be approximately uniformly distributed in the liquid, but difficulty in lofting higher-density particles was observed. Results such as these are essential to the development of accurate phase interaction models for three-phase flows; the implication of the present results for flow modeling is that an effective two-phase description may be accurate for describing the three-phase flows studied here.

With the successful combination of EIT and GDT reported here, additional investigations are now possible to help develop three-phase flow models for bubble-column reactor design. Future efforts will focus on extension of the EIT technique to Sandia's 48.26-cm diameter slurry bubble-column reactor

(SBCR) testbed and to other industrial-scale systems (*e.g.*, conducting vessels with insulating liquids). Further modifications might also include extending the resistive electrical technique to a capacitive technique that would increase the number of choices for each phase (for example, a nonconducting fluid).

Acknowledgments --- This work was performed at Sandia National Laboratories. Sandia is a multiprogram laboratory operated by Sandia Corporation, a Lockheed Martin Company, for the United States Department of Energy under Contract DE-AC04-94AL85000. A portion of this work was funded by the Federal Energy Technology Center under Field Work Proposal FEW 8616. The authors are grateful for technical interactions with B. A. Toseland of Air Products and Chemicals, Inc. The authors would also like to thank C. B. Lafferty and W. C. Ginn for their skilled technical assistance, D. R. Adkins for his early work with the GDT system, A. T. Leger for her early work with the EIT system, R. R. Lagasse for performing particle size analysis, and N. B. Jackson for her technical discussions related to catalysis.

REFERENCES

Ceccio, S. L., and George, D. L. (1996) A review of electrical impedance techniques for the measurement of multiphase flows. *J. Fluids Eng.* **118**, 391-399.

Dickin, F. J., Williams, R. A., and Beck, M. S. (1993) Determination of composition and motion of multicomponent mixtures in process vessels using electrical impedance tomography — I. Principles and process engineering applications. *Chem. Eng. Sci.* **48**, 1883-1897.

George, D. L., Ceccio, S. L., O'Hern, T. J., Shollenberger, K. A., and Torczynski, J. R. (1998a) Advanced material distribution measurement in multiphase flows: a case study, *Proceedings of the 1998 ASME Int. Mechanical Engineering Conference and Exposition, ASME*, FED-Vol. **247**, 31-42.

George, D. L., Ceccio, S. L., Shollenberger, K. A., Torczynski, J. R., and O'Hern, T. J. (1998b) Comparison of electrical-impedance tomography and gamma-densitometry tomography for the measurement of gas volume fraction profiles in a bubble column. *Proceedings of the 1998 ASME Fluids Engineering Division Summer Meeting*, FED-Vol. **245**, No. 98-5081.

George, D. L., Torczynski, J. R., Shollenberger, K. A., O'Hern, T. J. , and Ceccio, S. L. (2000) Validation of electrical-impedance tomography for measurements of material distribution in two-phase flows. Accepted for publication in the *Int. J. Multiphase Flow* **26**, 4.

Hewitt, G. F. (1978) *Measurement of Two-Phase Flow Parameters*, Academic Press, London.

Jackson, N. B., Torczynski, J. R., Shollenberger, K. A., O'Hern, T. J., and Adkins, D. R. (1996) Hydrodynamic characterization of slurry bubble-column reactors for Fischer-Tropsch synthesis.

Proceedings of the Thirteenth Annual Int. Pittsburgh Coal Conference, Vol. 2: Coal-Energy and the Environment, 1226-1231.

Jones, O. C., Lin, J.-T., and Ovacik, L. (1992) Investigation of electrical impedance imaging relative to two-phase, gas-liquid flows. *Chem. Eng. Comm.* **118**, 299-325.

Jones, O. C., Lin, J.-T., Ovacik, L., and Shu, H. (1993) Impedance imaging relative to gas-liquid systems. *Nucl. Eng. Design* **141**, 159-176.

Jones, O. C., Lin, J. T., Shu, H., Ovacik, L., and He, Y. (1994) Impedance imaging relative to binary mixtures. *Fifth Int. Symposium on Liquid-Solid Flows,* ASME.

Joshi, J. B., Parasu Veera, U., Prasad, Ch. V. Phanikumar, D. V., Deshphande, N. S., Thakre, S. S., and Thorat, B. N. (1998) Gas hold-up structure in bubble column reactors. *PINSA* **64 A**, 4, 441-567.

Kumar, S. B., Moslemian, D., and Dudukovic, M. P., (1995) A gamma-ray tomographic scanner for imaging voidage distribution in 2-phase flow systems. *Flow Measurement and Instrumentation* **6**, 61-73.

Lamarsh, J. R. (1983) *Introduction to Nuclear Engineering,* Addison-Wesley, Reading, MA, pp. 78-88, 472-488, 648-649.

Maxwell, J. C. (1881) *A Treatise on Electricity and Magnetism,* Clarendon Press, Oxford, England.

Mwambela, A. J., Kirkedam, E., Johansen, G. A., and Isaksen, O. (1997) Reconstruction of capacitance tomography data using global entropic thresholding methods: experimental validation. *Frontiers in Industrial Process Tomography II,* Proceedings of Engineering Foundation Conference.

O'Hern, T. J., Torczynski, J. R., Ceccio, S. L., Tassin, A. L., Chahine, G. L., Duraiswami, R., and Sarkar, K. (1995) Development of an electrical-impedance tomography system for an air-water vertical

bubble column. *ASME Forum on Measurement Techniques in Multiphase Flows*, FED-Vol. **233**, 531-537.

Plaskowski, A., Beck, M. S., Thorn, R., and Dyakowski, T. (1995) *Imaging Industrial Flows: Applications of Electrical Process Tomography,* Institute of Physics Publishing, Bristol, England.

Shollenberger, K. A., Torczynski, J. R., Adkins, D. R., O'Hern, T. J., and Jackson, N. B. (1997a) Gamma-densitometry tomography of gas holdup spatial distribution in industrial-scale bubble columns. *Chem. Eng. Sci.* **52**, 2037-2048.

Shollenberger, K. A., Torczynski, J. R, O'Hern, T. J., Adkins, D. R., Ceccio, S. L., and George, D. L. (1997b) Comparison of gamma-densitometry tomography and electrical-impedance tomography for determining material distribution in liquid-solid flows. *Proceedings of the 1997 ASME Fluids Engineering Division Summer Meeting*, Vol. FEDSM '97, No. 97-3690.

Thomas, D. G. (1965) Transport characteristics of suspension: VIII. A note on the viscosity of Newtonian suspensions of uniform spherical particles. *J. Colloid Science* **20**, 267-277.

Thoraeus, R. (1965) Attenuation of gamma radiation from ^{60}Co, ^{137}Cs, ^{192}Ir, and ^{226}Ra in various materials used in radiology. *Acta Radiologica* **3**, 81-86.

Torczynski, J. R., O'Hern, T. J., Shollenberger, K. A., Ceccio, S. L., and Tassin, A. L. (1996a) Finite element method electrical-impedance tomography for phase distribution determination in multiphase flows: validation calculations and experiments. *ASME Cavitation and Multiphase Flow Forum,* FED-Vol. **236**, 497-501.

Torczynski, J. R., Adkins, D. R., Shollenberger, K. A., and O'Hern, T. J. (1996b) Application of gamma-densitometry tomography to determine phase spatial variation in two-phase and three-phase bubbly flows. *ASME Cavitation and Multiphase Flow Forum,* FED-Vol. **236**, 503-508.

Torczynski, J. R., O'Hern, T. J., Adkins, D. R., Jackson, N. B., and Shollenberger, K. A. (1997) *Advanced Tomographic Flow Diagnostics for Opaque Multiphase Fluids*, Report SAND97-1176, Sandia National Laboratories, Albuquerque, NM.

Vest, C. M. (1985) Tomography for properties of materials that bend rays: a tutorial. *Appl. Opt.* **24**, 4089-4094.

Yorkey, T. J., Webster, J. G., and Tompkins, W. J. (1987) Comparing reconstruction methods for electrical impedance tomography. *IEEE Trans. Biomedical Eng.* **11**, 843-852.

Table 1. Properties of the materials used in the three-phase experiments.

material	ρ (g/cm^3)	μ (cm^{-1})	σ (μS/cm)	ω (μF/cm)
polystyrene	1.04	0.0866	$< 10^{-10}$	2.3×10^{-7}
glass	2.41	0.209	5.9×10^{-11}	$\approx 5 \times 10^{-7}$
water/$NaNO_3$	0.997	0.0856	242 - 432	$\approx 7 \times 10^{-6}$
air	0.00106	0.0000819	$\approx 10^{-10}$	8.86×10^{-8}

Table 2. Average gas volume fractions for three-phase experiments from the EIT/GDT system.

Particle Type		U_G (cm/s)						
	$\bar{\varepsilon}_S^{nom}$	2.9	5.8	8.8	11.7	17.5	23.4	29.2
40-100 μm	0.00			0.181	0.214	0.263	0.304	
glass	0.05	a	a	0.141	0.185	0.242	0.283	
	0.10	a	a	0.144	0.197	0.244	0.282	
	0.15	a	a	a	0.168	0.223	0.268	
120-200 μm	0.00					0.246	0.290	0.321
glass	0.05	a	a	a	a	0.245	0.280	0.317
	0.10	a	a	a	a	0.229	0.277	0.307
	0.15	a	a	a	a	0.231	0.267	0.298
170-260 μm	0.00	0.090	0.149	0.193	0.220	0.256	0.288	
polystyrene	0.05	0.101	0.166	0.199	0.221	0.256	0.283	
	0.10	0.106	0.177	0.216	0.243	0.279	0.308	
	0.15	f	0.171	0.213	0.242	0.275	0.298	
200-700 μm	0.00	0.089	0.147	0.190	0.222			
polystyrene	0.05	0.088	0.143	0.179	0.207			
	0.10	0.089	0.147	0.180	0.210			
	0.22	0.090	0.152	0.181	0.207			
	0.30	f	0.149	0.189	0.215			
water	0.00	0.075	0.117	0.137	0.167	0.213	0.249	

a = air flow rate inadequate to loft all solids

f = head of foam from surfactant in particle coating expanded to top of column

Figure 1. Schematic diagram of GDT system applied to a circular domain showing lateral and radial coordinate systems.

Figure 2. Conceptual diagram of an EIT system applied to a circular domain.

Figure 3. EIT strip electrode array. The bottom scale is in inches.

Figure 4. Schematic diagram of Lexan bubble column (19-cm I.D.) used in three-phase flow experiments showing measurement locations.

Figure 5. Size distribution of medium polystyrene beads (diameter 170 – 260 μm, density 1.04 g/cm^3).

Figure 6. Size distribution of large polystyrene beads (diameter 200 – 700 μm, density 1.04 g/cm^3).

Figure 7. Size distribution of small glass beads (diameter 40 – 100 μm, density 2.41 g/cm^3).

Figure 8. Size distribution of medium glass beads (diameter 120 – 200 μm, density 2.41 g/cm^3).

Figure 9. Comparison of nominal slurry concentration, $\bar{\varepsilon}_s^{nom}$, and slurry concentration at measurement plane from combined GDT/EIT measurements.

Figures 10 (a)-(d). Phase volume fraction profiles as a function of superficial gas velocity: (a) 5.8 cm/s, (b) 11.7 cm/s, (c) 17.5 cm/s, and (d) 23.4 cm/s. The solid phase is 170-260 μm polystyrene beads at a nominal slurry concentration of 0.10.

Figures 11 (a)-(d). Phase volume fraction profiles as a function of nominal slurry concentration, $\bar{\varepsilon}_s^{nom}$: (a) 0.00, (b) 0.05, (c) 0.10, and (d) 0.15. The superficial gas velocity is 17.5 cm/s and the solid phase is 120-200 μm glass beads.

Figure 12. Phase volume fraction profiles where the solid phase is 40-100 μm glass beads, the superficial gas velocity is 17.5 cm/s, and the nominal slurry concentration is 0.10.

Figure 13. Phase volume fraction profiles where the solid phase is 200-700 μm polystyrene beads, the superficial gas velocity is 11.7 cm/s, and the nominal slurry concentration is 0.10.

Figure 14. Radially-averaged gas volume fraction as a function of superficial gas velocity.

Figure 15. Gas volume fraction as a function of nominal slurry concentration, $\bar{\varepsilon}_S^{nom}$, for glass particles: 40-100 μm particles are open symbols and the 120-200 μm particles are closed symbols. The solid lines are the correlation of Equation 24.

Figure 16. Gas volume fraction as a function of nominal slurry concentration, $\bar{\varepsilon}_S^{nom}$, for polystyrene particles: 170-260 μm particles are open symbols and the 200-700 μm particles are closed symbols. The solid lines are the correlation of Equation 24.

Figure 1.

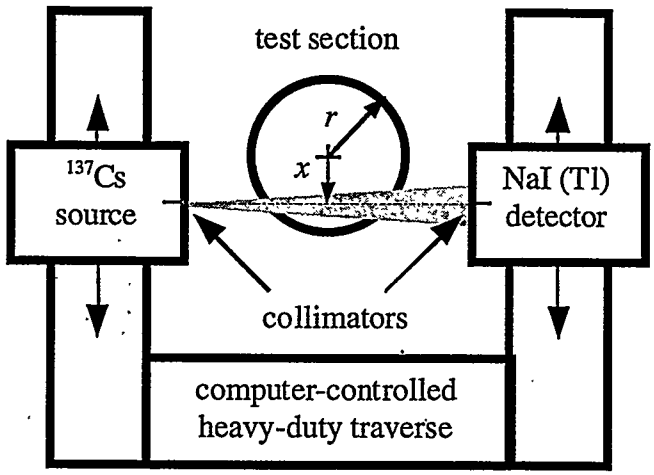
test section
r
x
^{137}Cs
source
NaI (Tl)
detector
collimators
computer-controlled
heavy-duty traverse

Figure 2.

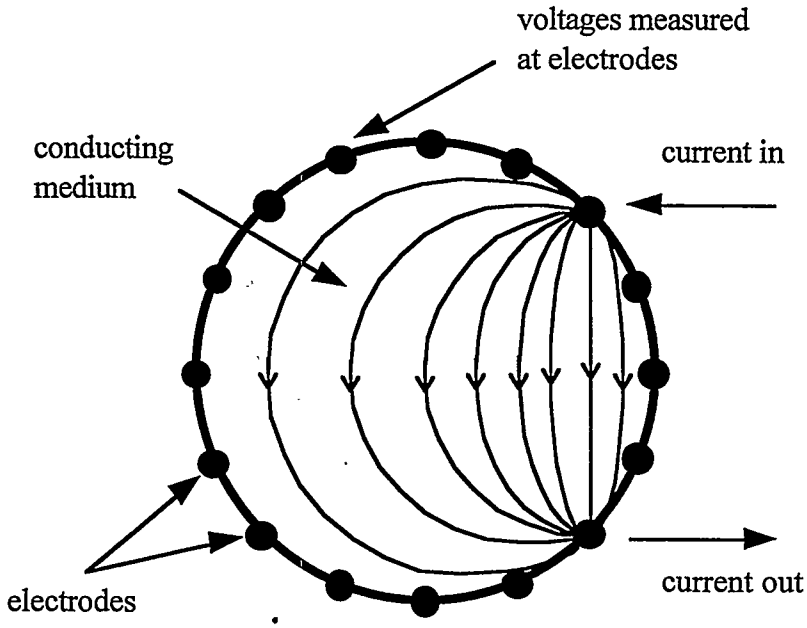
voltages measured
at electrodes
conducting
medium
current in
electrodes
current out

Figure 3.

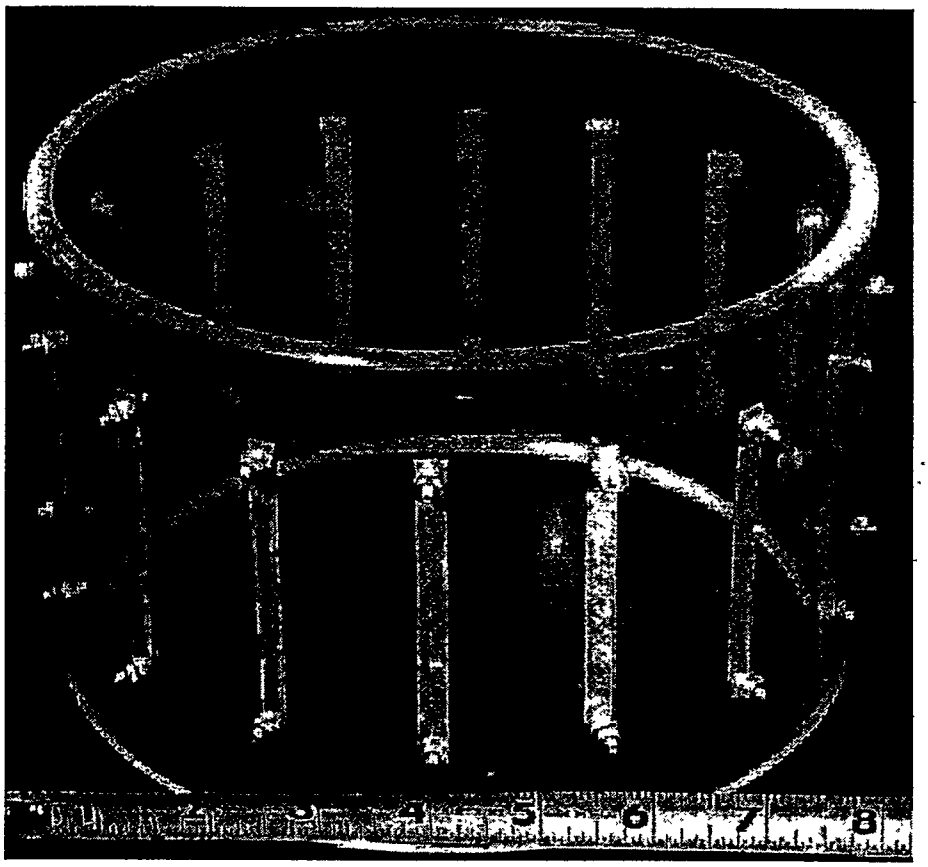

Figure 4.

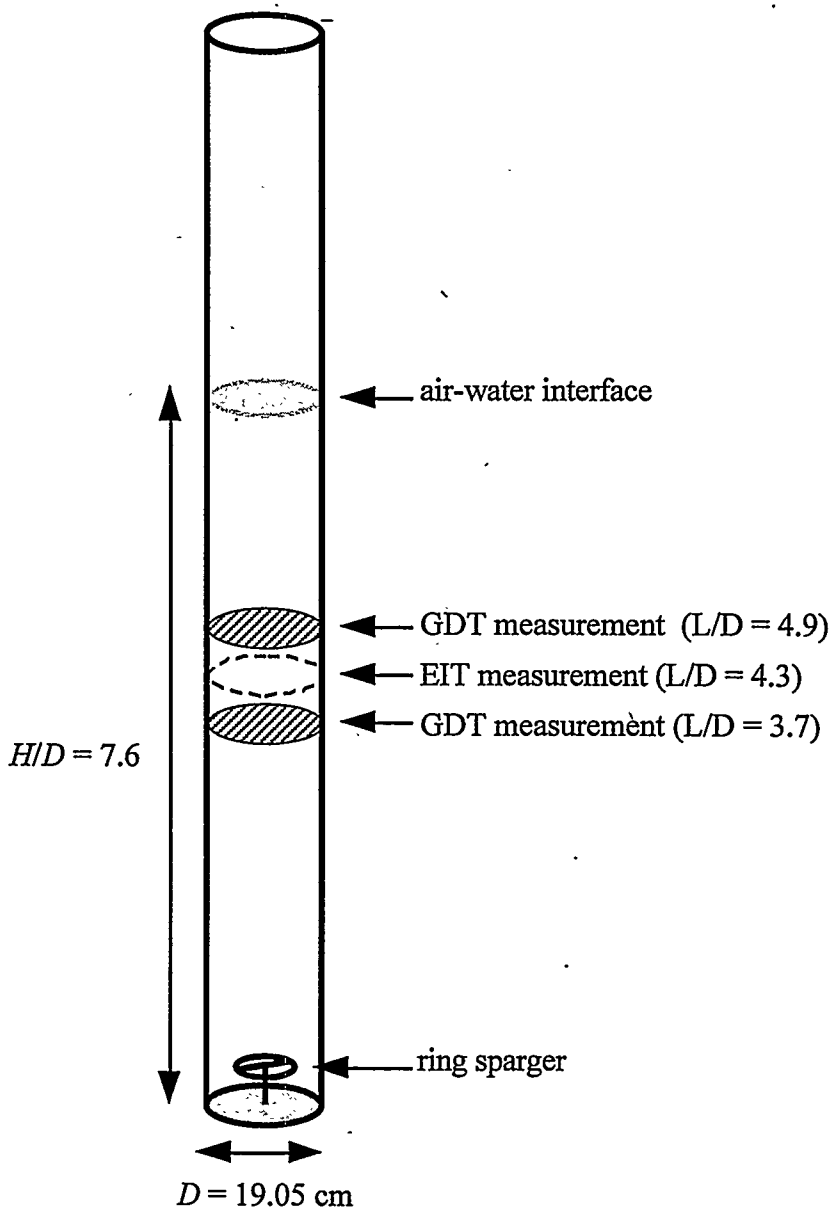
air-water interface
GDT measurement (L/D = 4.9)
EIT measurement (L/D = 4.3)
GDT measurement (L/D = 3.7)
H/D = 7.6
ring sparger
D = 19.05 cm

Figure 5.

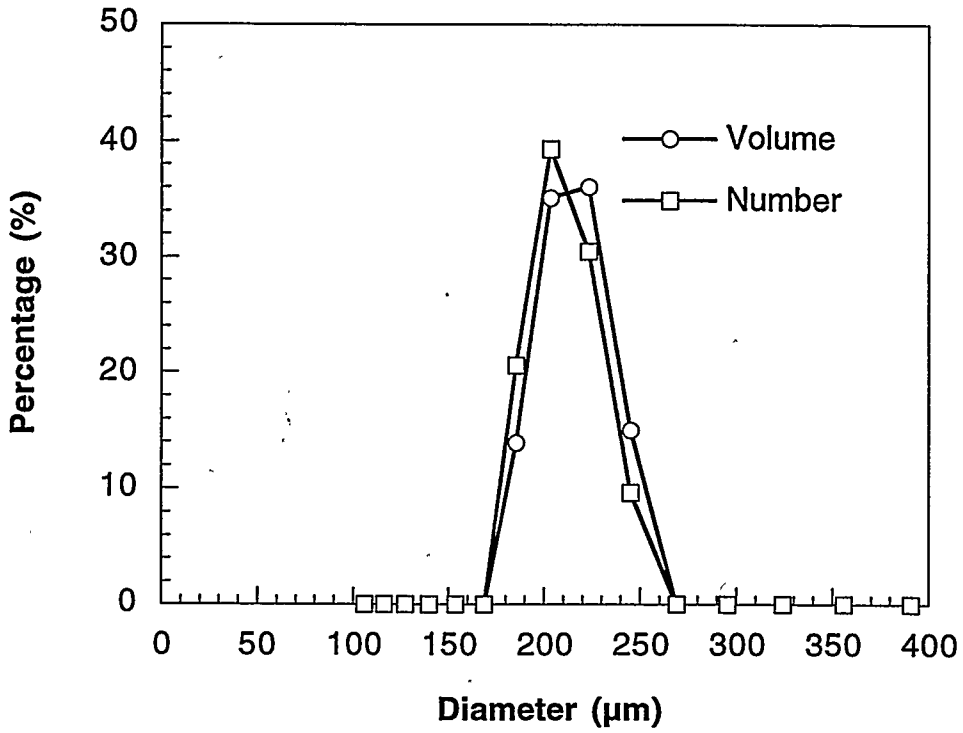
50
40
30
20
10
0
Percentage (%)
Volume
Number
0
50
100
150
200
250
300
350
400
Diameter (μm)

Figure 6.

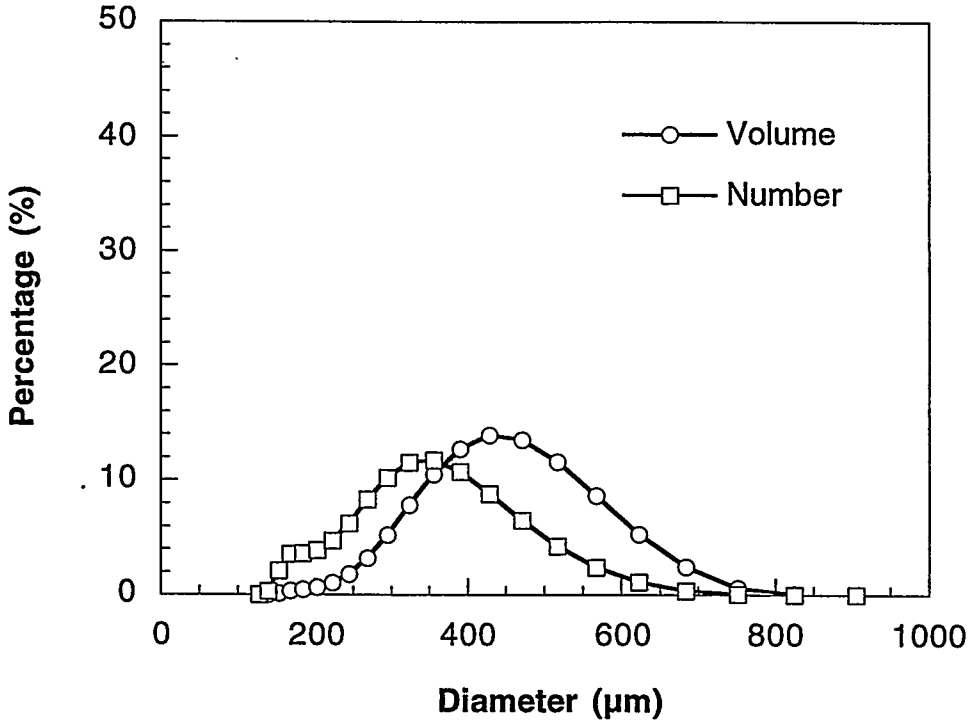
50
40
30
20
10
0
Percentage (%)
Volume
Number
0
200
400
600
800
1000
Diameter (μm)

Figure 7.

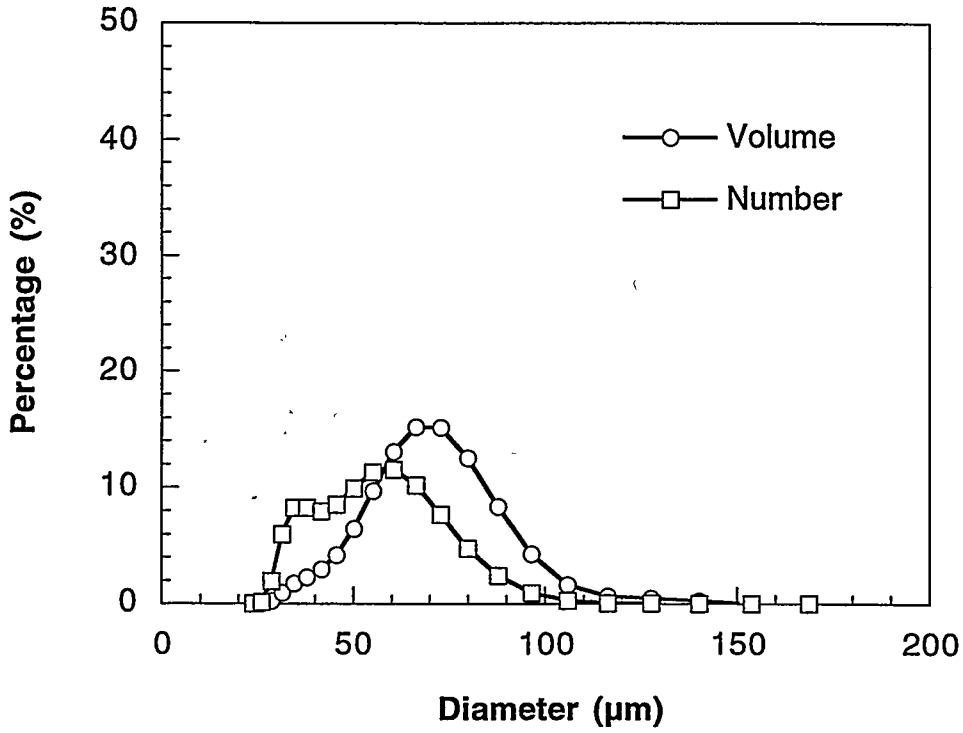
50
40
30
20
10
0
Percentage (%)
Volume
Number
0
50
100
150
200
Diameter (μm)

Figure 8.

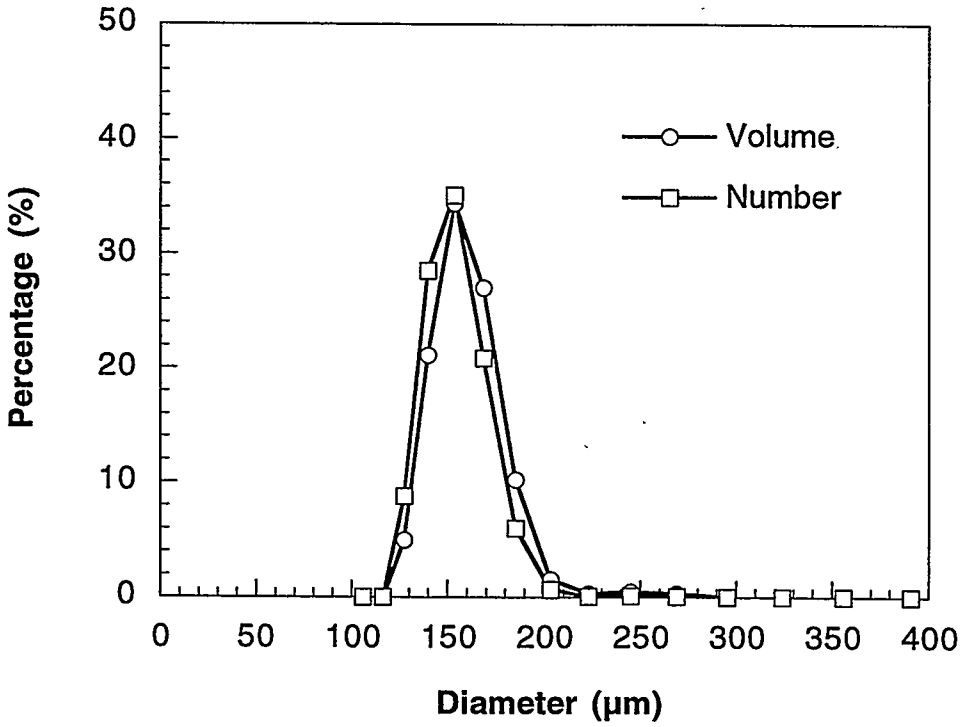
50
40
30
20
10
0
Percentage (%)
Volume
Number
0
50
100
150
200
250
300
350
400
Diameter (μm)

Figure 9.

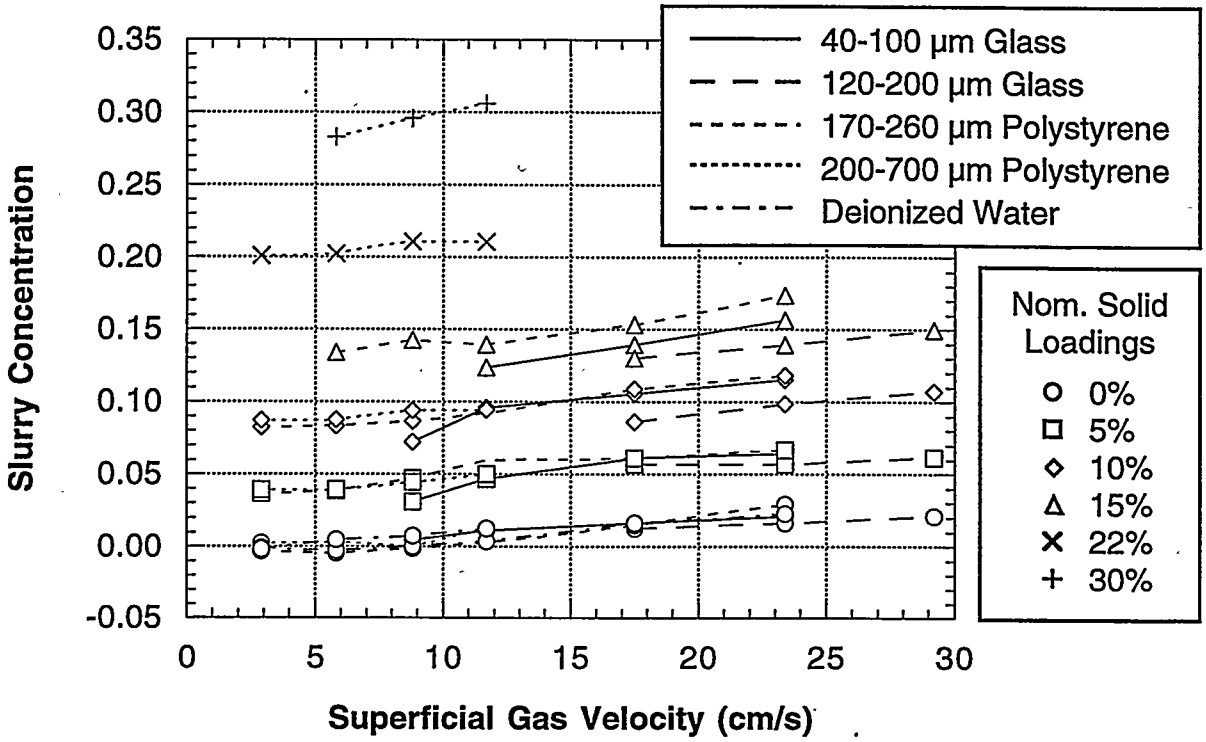
Slurry Concentration
0.35
0.30
0.25
0.20
0.15
0.10
0.05
0.00
-0.05
0
5
10
15
20
25
30
Superficial Gas Velocity (cm/s)
40-100 µm Glass
120-200 µm Glass
170-260 µm Polystyrene
200-700 µm Polystyrene
Deionized Water
Nom. Solid Loadings
0%
5%
10%
15%
22%
30%

Figure 10 (a).

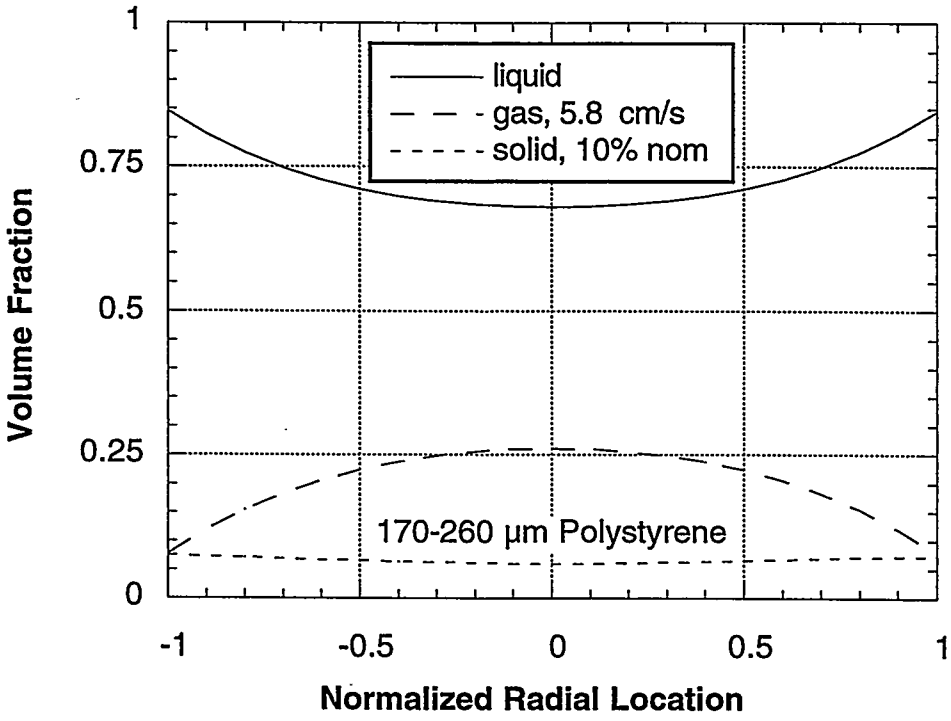
liquid
gas, 5.8 cm/s
solid, 10% nom
170-260 µm Polystyrene
Volume Fraction
Normalized Radial Location
1
0.75
0.5
0.25
0
-1
-0.5
0
0.5
1

Figure 10 (b).

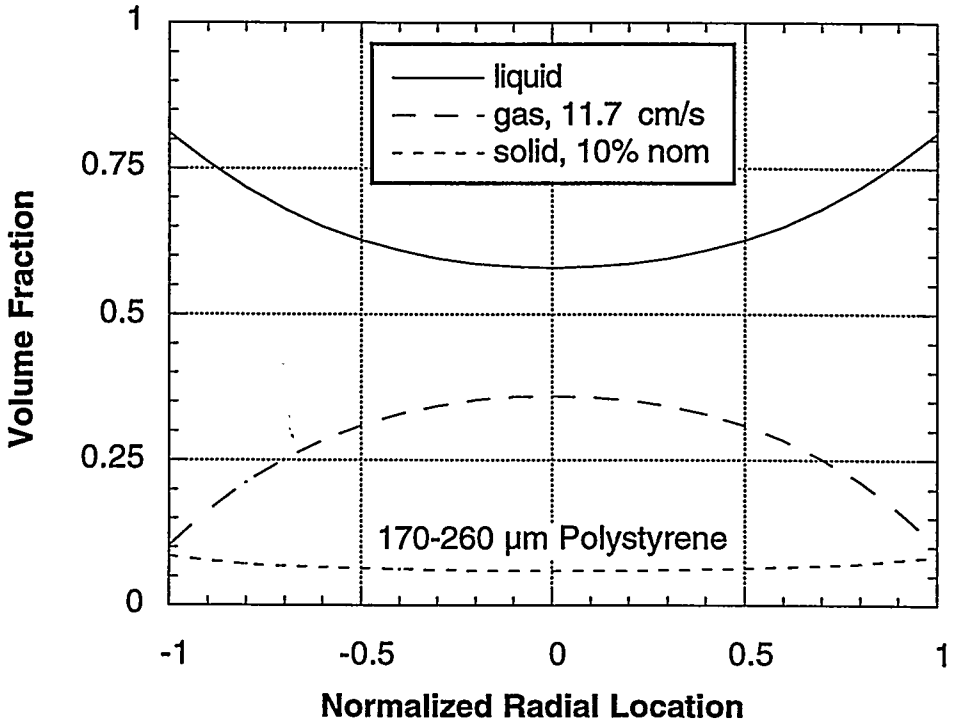
liquid
gas, 11.7 cm/s
solid, 10% nom
170-260 µm Polystyrene
Volume Fraction
Normalized Radial Location
1
0.75
0.5
0.25
0
-1
-0.5
0
0.5
1

Figure 10 (c).

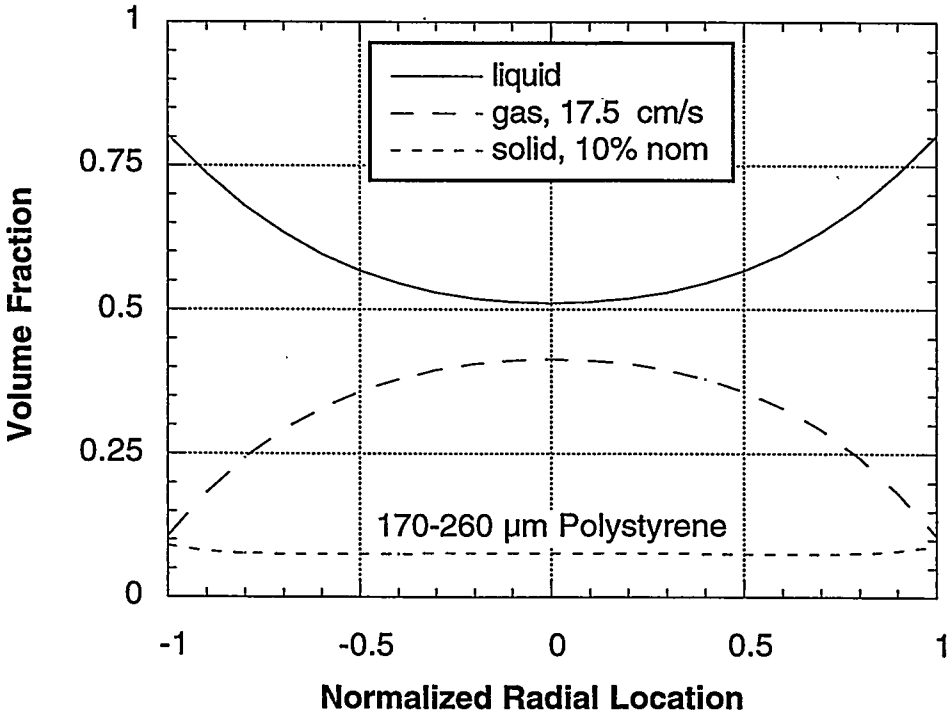
liquid
gas, 17.5 cm/s
solid, 10% nom
170-260 µm Polystyrene
Volume Fraction
Normalized Radial Location
1
0.75
0.5
0.25
0
-1
-0.5
0
0.5
1

Figure 10 (d).

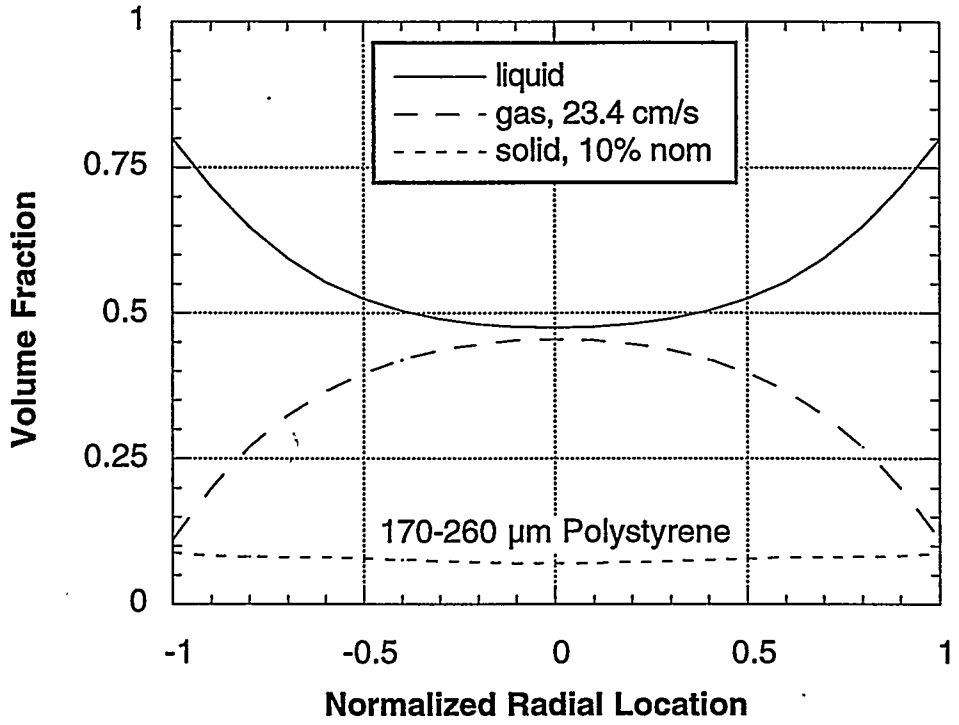
liquid
gas, 23.4 cm/s
solid, 10% nom
170-260 µm Polystyrene
Volume Fraction
Normalized Radial Location
1
0.75
0.5
0.25
0
-1
-0.5
0
0.5
1

Figure 11 (a).

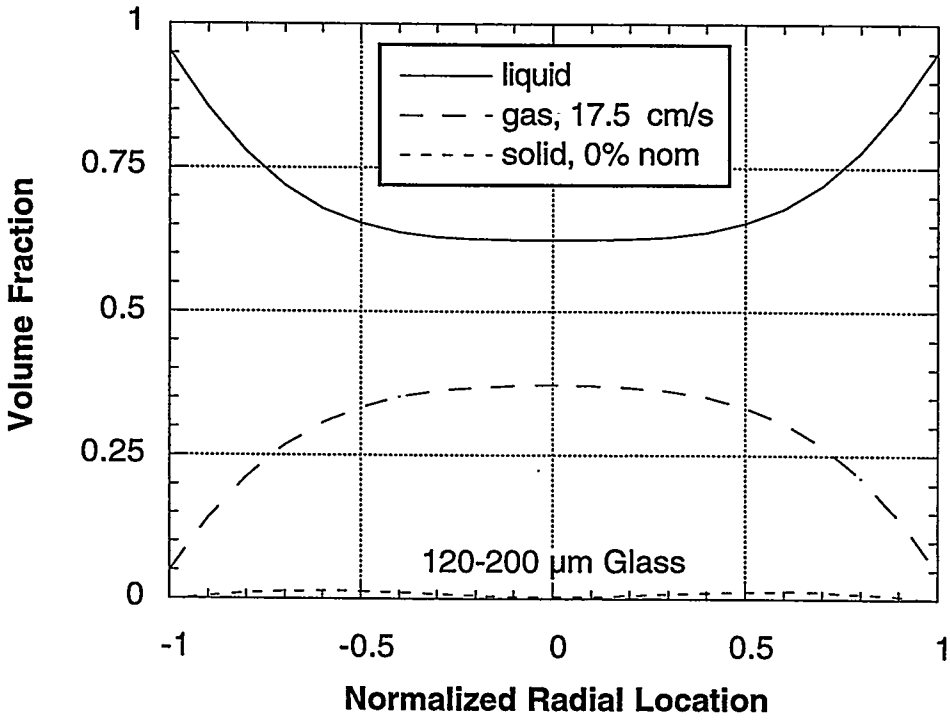
liquid
gas, 17.5 cm/s
solid, 0% nom
120-200 µm Glass
Volume Fraction
Normalized Radial Location
1
0.75
0.5
0.25
0
-1
-0.5
0
0.5
1

Figure 11 (b).

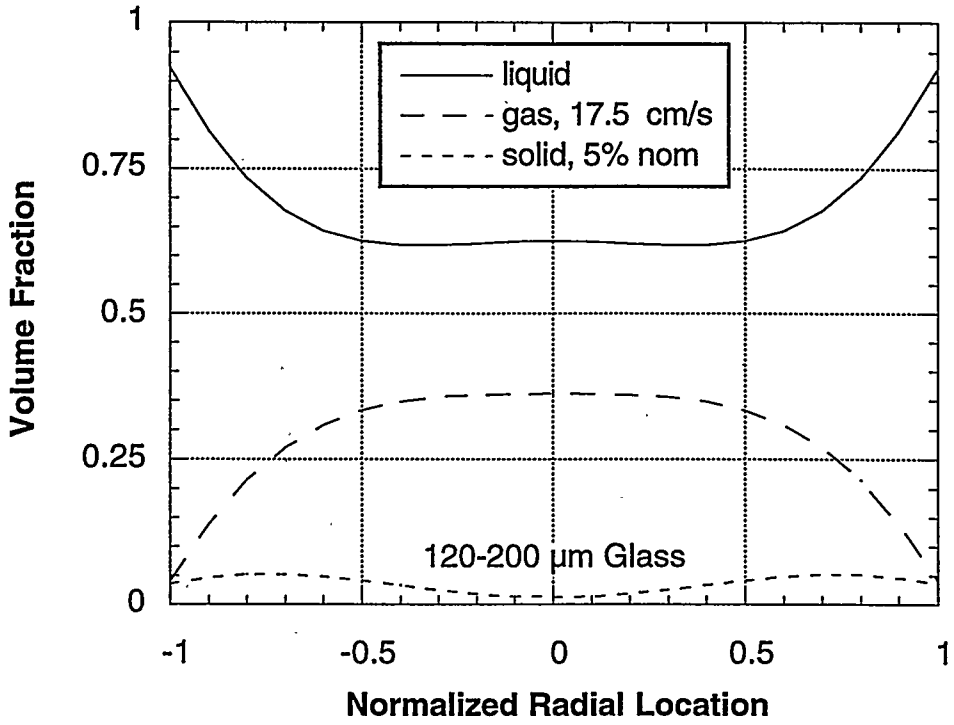
liquid
gas, 17.5 cm/s
solid, 5% nom
120-200 µm Glass
Volume Fraction
Normalized Radial Location
1
0.75
0.5
0.25
0
-1
-0.5
0
0.5
1

Figure 11 (c).

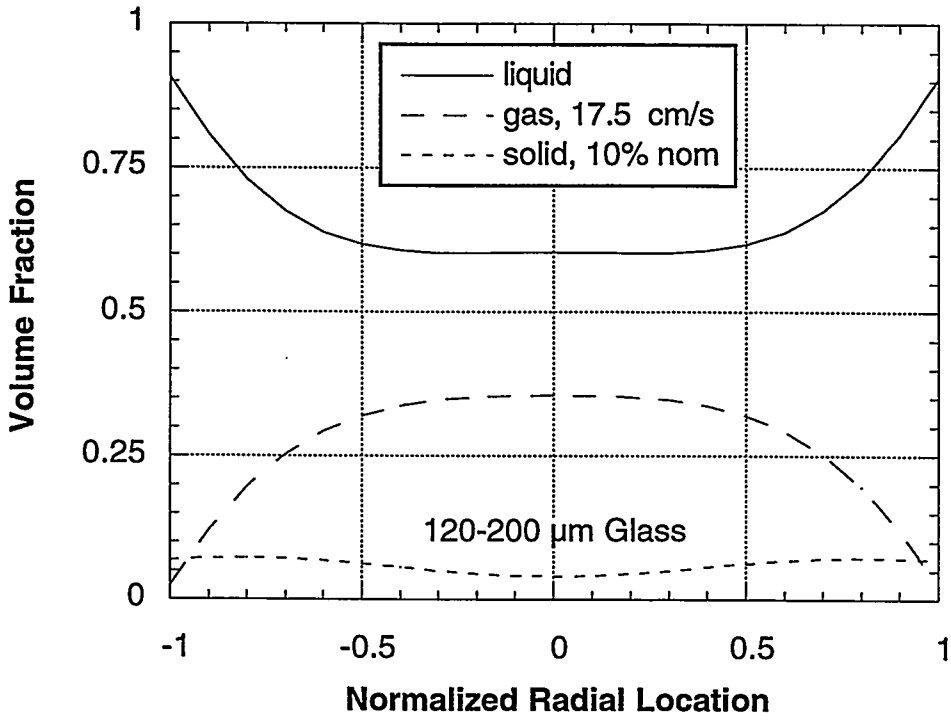
liquid
gas, 17.5 cm/s
solid, 10% nom
120-200 µm Glass
Volume Fraction
Normalized Radial Location
1
0.75
0.5
0.25
0
-1
-0.5
0
0.5
1

Figure 11 (d).

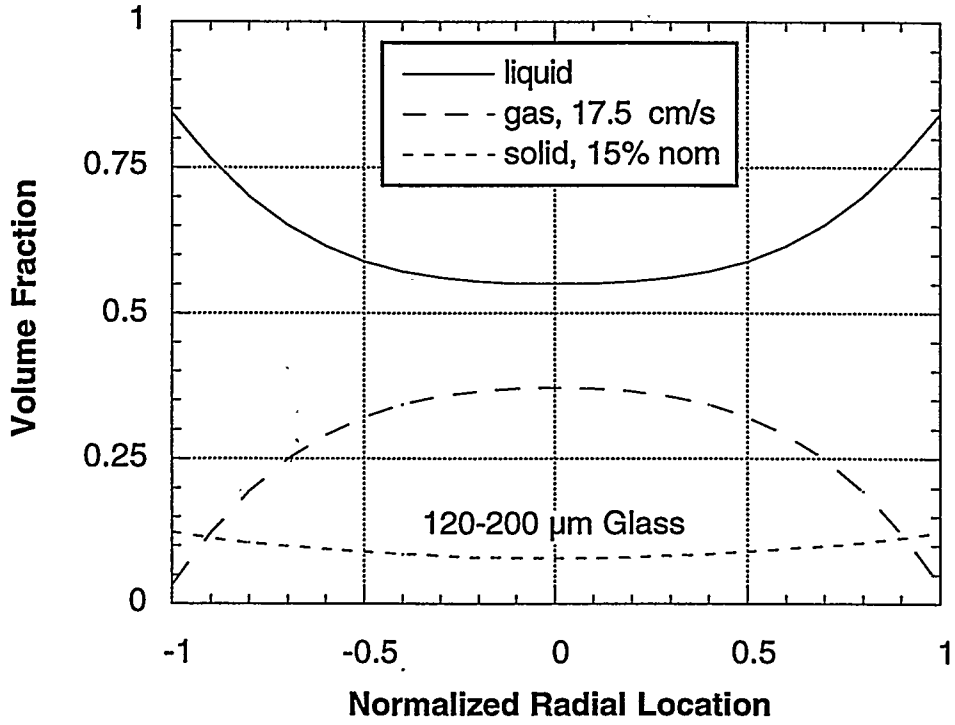
liquid
gas, 17.5 cm/s
solid, 15% nom
120-200 µm Glass
Volume Fraction
Normalized Radial Location
1
0.75
0.5
0.25
0
-1
-0.5
0
0.5
1

Figure 12.

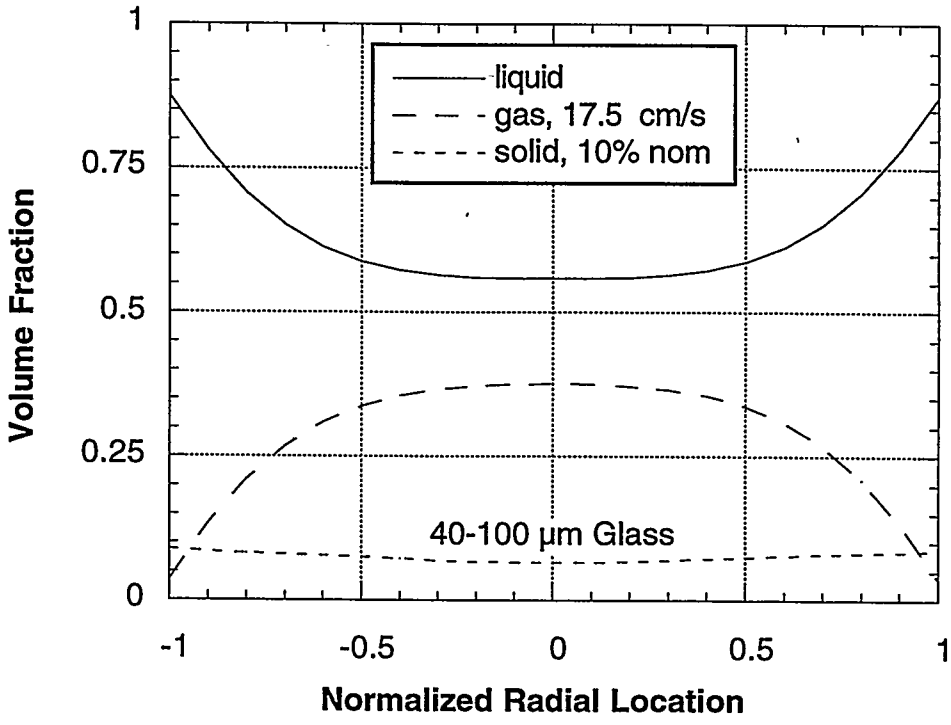
liquid
gas, 17.5 cm/s
solid, 10% nom
40-100 µm Glass
Volume Fraction
Normalized Radial Location
1
0.75
0.5
0.25
0
-1
-0.5
0
0.5
1

Figure 13.

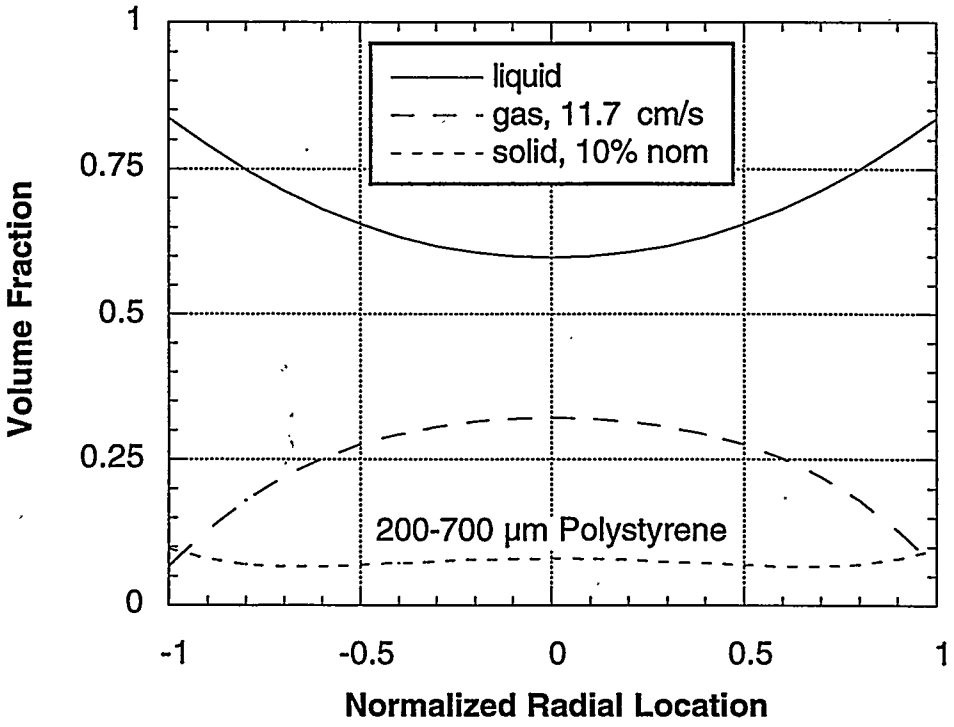
liquid
gas, 11.7 cm/s
solid, 10% nom
200-700 µm Polystyrene
Volume Fraction
Normalized Radial Location
1
0.75
0.5
0.25
0
-1
-0.5
0
0.5
1

Figure 14.

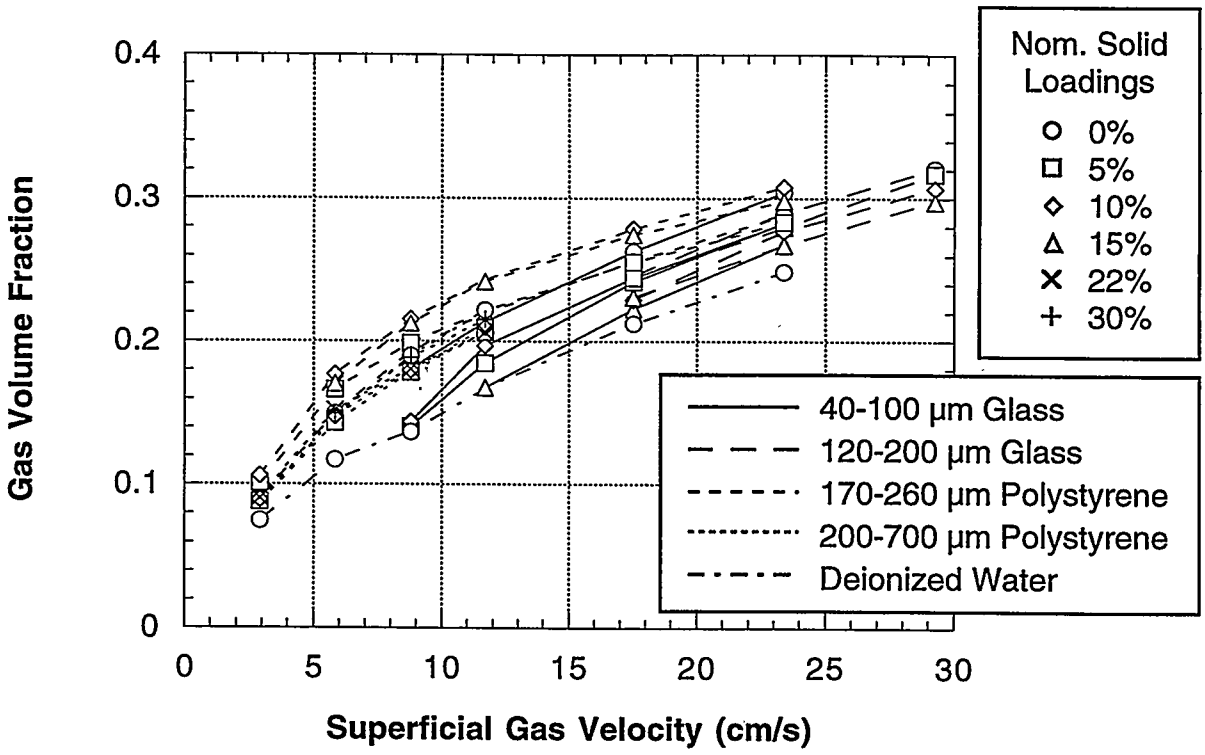
Gas Volume Fraction
0.4
0.3
0.2
0.1
0
0
5
10
15
20
25
30
Superficial Gas Velocity (cm/s)
Nom. Solid Loadings
0%
5%
10%
15%
22%
30%
40-100 µm Glass
120-200 µm Glass
170-260 µm Polystyrene
200-700 µm Polystyrene
Deionized Water

Figure 15.

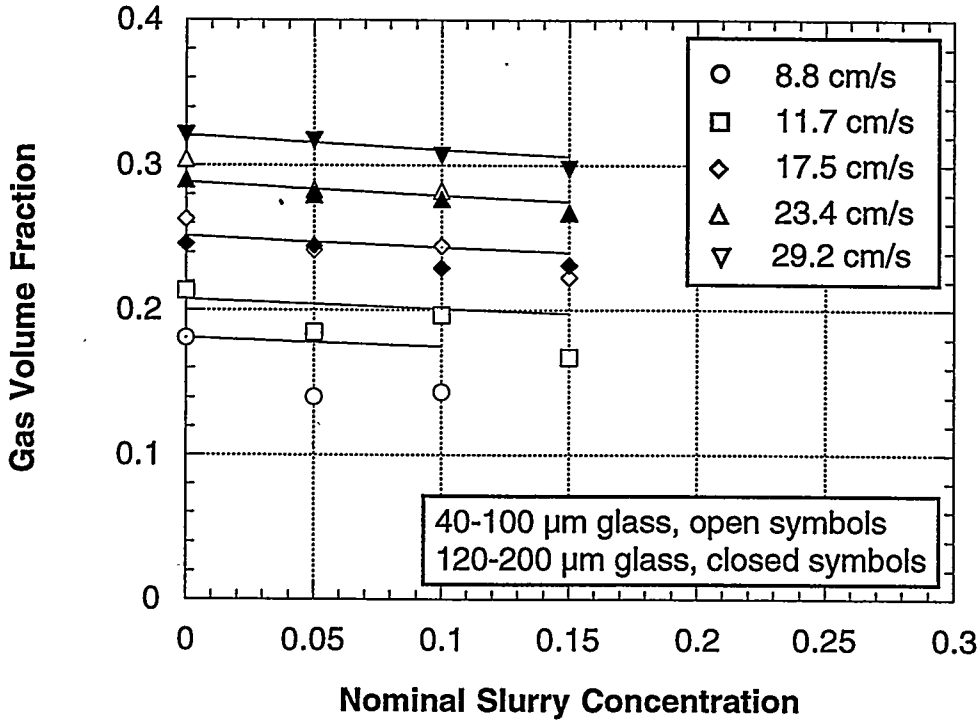
Gas Volume Fraction
0.4
0.3
0.2
0.1
0
0
0.05
0.1
0.15
0.2
0.25
0.3
Nominal Slurry Concentration
8.8 cm/s
11.7 cm/s
17.5 cm/s
23.4 cm/s
29.2 cm/s
40-100 µm glass, open symbols
120-200 µm glass, closed symbols

Figure 16.

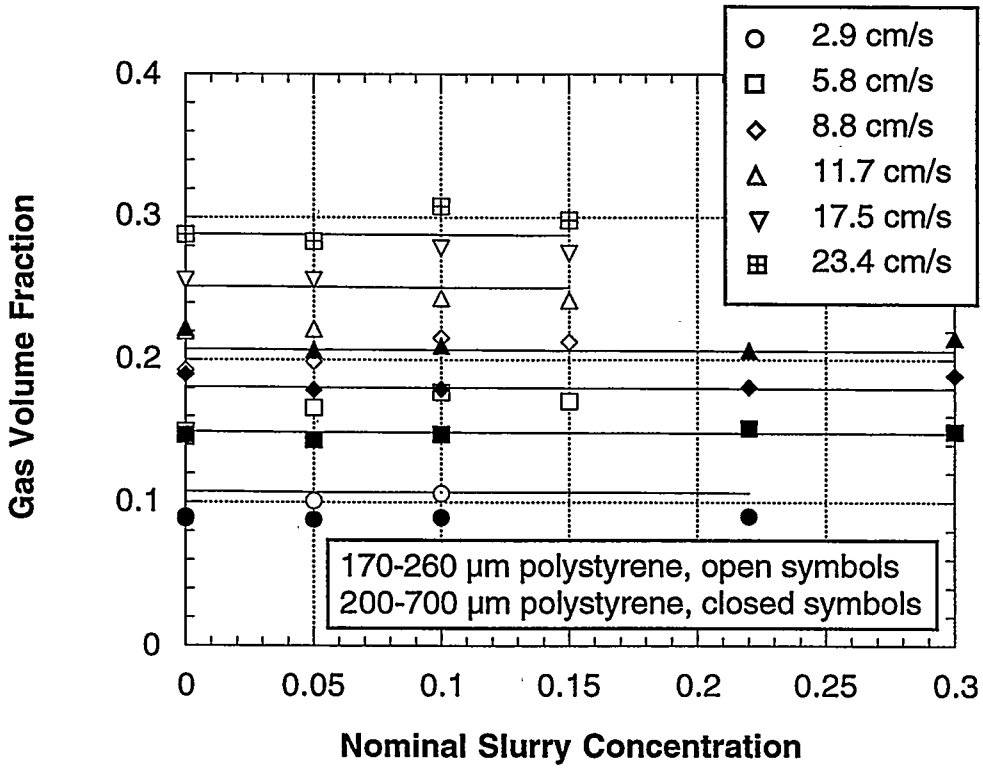
2.9 cm/s
5.8 cm/s
8.8 cm/s
11.7 cm/s
17.5 cm/s
23.4 cm/s
170-260 µm polystyrene, open symbols
200-700 µm polystyrene, closed symbols
Gas Volume Fraction
Nominal Slurry Concentration
0
0.1
0.2
0.3
0.4
0.05
0.15
0.25